American Mineralogist, Volume 84, pages 1741–1759, 1999

The application of electron backscatter diffraction and orientation contrast imaging in the SEM to textural problems in rocks

DAVID J. PRIOR,[1,*] ALAN P. BOYLE,[1] FRANK BRENKER,[2] MICHAEL C. CHEADLE,[1] AUSTIN DAY,[3] GLORIA LOPEZ,[4] LUCA PERUZZO,[6] GRAHAM J. POTTS,[1] STEVE REDDY,[5] RICHARD SPIESS,[6] NICK E. TIMMS,[7] PAT TRIMBY,[8] JOHN WHEELER,[1] AND LENA ZETTERSTRÖM[9]

[1]Department of Earth Sciences, Liverpool University, L69 3BX, U.K.
[2]Institut für Mineralogie und Geochemie, Universität zu Köln, Zülpicher Strasse 49b, 50674 Köln, Germany
[3]HKL technology, Blåkildevej 17k, 9500 Hobro, Denmark
[4]Departamento de Geología, Universidad de Chile, Santiago, Chile
[5]Tectonics Special Research Centre, School of Applied Geology, Curtin University of Technology, Perth, WA 6102, Australia
[6]Department of Mineralogy and Petrology, University of Padua, Italy
[7]Department of Geology, James Cook University, Townsville, Australia
[8]Department of Geology, Utrecht University, Utrecht, Netherlands
[9]Laboratory for Isotope Geology, Swedish Museum of Natural History, Stockholm, Sweden

ABSTRACT

In a scanning electron microscope (SEM) an electron beam sets up an omni-directional source of scattered electrons within a specimen. Diffraction of these electrons will occur simultaneously on all lattice planes in the sample and the backscattered electrons (BSE), which escape from the specimen, will form a diffraction pattern that can be imaged on a phosphor screen. This is the basis of electron backscatter diffraction (EBSD). Similar diffraction effects cause individual grains of different orientations to give different total BSE. SEM images that exploit this effect will show orientation contrast (OC). EBSD and OC imaging are SEM-based crystallographic tools.

EBSD enables measurement of the crystallographic orientation of individual rock-forming minerals as small as 1 μm, and the calculation of misorientation axes and angles between any two data points. OC images enable mapping of all misorientation boundaries in a specimen and thus provide a location map for EBSD analyses. EBSD coupled to OC imaging in the SEM enables complete specimen microtextures and mesotextures to be determined. EBSD and OC imaging can be applied to any mineral at a range of scales and enable us to expand the microstructural approach, so successful in studies of quartz rocks, for example, to the full range of rock-forming minerals. Automated EBSD analysis of rocks remains problematic, although continuing technical developments are enabling progress in this area.

EBSD and OC are important new tools for petrologists and petrographers. Present and future applications of EBSD and OC imaging include phase identification, studying deformation mechanisms, constraining dislocation slip systems, empirical quantification of microstructures, studying metamorphic processes, studying magmatic processes, and constraining geochemical microsampling. In all these cases, quantitative crystallographic orientation data enable more rigorous testing of models to explain observed microstructures.

INTRODUCTION

A complete petrographic description of any rock comprises observations at the centimetre to angstrom scale, against which petrogenetic models are tested. Such data underpin many aspects of earth sciences. Petrographic observations include (1) spatial distribution, size and shape of phases; (2) the composition of phases and the variation of composition within phases; (3) the crystallographic orientations of phases and variation of orientation within phases; (4) the geometry and structure of subgrain boundaries; (5) the geometry and structure of boundaries between grains of the same phase; and (6) the geometry and structure of boundaries between different phases; and the geometry and structure of triple junctions.

By virtue of widespread availability, low cost, and versatility, transmitted and reflected light microscopy have served, and will continue to serve, as the mainstay of petrographic data collection. However, some data are inaccessible using light optics and, increasingly, more demanding scientific objectives necessitate that certain data be collected with greater thoroughness and precision than is possible with light microscopy.

*E-mail: davep@liverpool.ac.uk

0003-004X/99/1112–1741$05.00

BSE imaging (Lloyd 1985) together with X-ray microanalysis (Goldstein et al. 1992) in the SEM provide (1) images of rock textures with sub-micrometer spatial resolution, based on contrasts between materials of different composition (atomic number or Z-contrast) and (2) qualitative and quantitative microchemical data with micrometer resolution. With modern hardware and software developments, these techniques have become commonplace in the analysis of rock textures.

OC imaging using forescatter detectors (Day 1993; Prior et al. 1996) and EBSD (Dingley 1984; Randle 1992; Wikinson and Hirsch 1997; Humphreys 1999) in the SEM provide: (1) images of rock textures with sub-micrometer spatial resolution, based on signal contrasts between materials with different crystallographic orientations or different crystallographic structures and (2) qualitative and quantitative crystallographic orientation data with micrometer resolution.

OC imaging and EBSD are relatively new techniques to the petrologist. They are of fundamental importance as many models that seek to explain rock microstructures have implications for the distribution of crystallographic orientations and are thus testable using SEM-based crystallographic data. This paper aims to review (1) the principles behind EBSD and OC imaging; (2) analytical procedures appropriate to rock specimens; and (3) some applications to hard-rock petrology and petrography.

ELECTRON BACKSCATTER DIFFRACTION

In the literature, EBSD is also called electron backscatter patterns (EBSP) and backscatter kikuchi diffraction. In this paper, EBSD refers to the diffraction technique and EBSP refers to individual diffraction patterns. The same diffraction process is exploited in transmission electron microscopy giving rise to kikuchi lines (Nishikawa and Kikuchi 1928; Loretto 1994), and in electron channeling in the SEM (Joy 1974; Lloyd 1987, 1994). A direct comparison of EBSD and electron channeling is given by Randle (1992) and Wilkinson and Hirsch (1997), and the reciprocity theorem linking the two techniques is detailed by Reimer et al. (1986). A comparison of EBSD and other electron optical techniques appears in Humphreys and Hatherley (1995). The following discussion uses both wave and particle descriptions of electrons.

When a high-energy electron of an electron beam is incident upon a sample, there are a variety of possible interactions; Goldstein et al. (1992), Loretto (1994), and the MATTER package all provide good reviews of these processes. The simplest interaction is elastic scattering, in which the incident electrons lose little energy. Incident electrons may also undergo inelastic scattering events, in which they lose significant portions of their energy. Elastic scattering changes the incident electron trajectory by between 0° and 180° and comprises two components: (1) coulombic interaction of the incident electron with a nucleus (Rutherford scattering) and (2) interaction with internucleic electron cloud (including inner and outer shell electrons and those in the conduction band).

Electrons that pass close to a nucleus will be scattered through larger angles than those that pass more distantly, reflecting a greater contribution from the interaction with the nucleus (Fig. 1a). The diameter of an electron beam probe (1 nm absolute minimum) is larger than atomic spacing (~0.1–0.3 nm). Thus, individual electrons will impact at all possible distances from nucleii of the specimen, so that the interaction of an incident beam and the specimen will give rise to a population of scattered electrons with all possible trajectories. The scattered electron intensities will be a function of scatter angle (Fig. 1b). This omni-directional population of scattered electrons acts as the source for EBSD in the SEM. For simplicity we will consider that the electrons radiate from a very small source volume (Fig. 1c) and that only one order of diffraction from each lattice plane is significant. In a two-dimensional section, there will be four trajectories that satisfy the Bragg condition for diffraction of each lattice plane (Fig. 1c):

$$n\lambda = 2d \sin\theta$$

where θ is the diffraction angle, n is an integer (order of diffraction), λ is the wavelength of the electron beam energy (correspondent to accelerating voltage) and d is the lattice spacing.

In three dimensions, the trajectories of electrons that satisfy the Bragg condition define two cones that, in turn, generate two cones of diffracted electrons (Fig. 1e). Every lattice plane generates two diffraction cones, although the intensity of diffraction depends on the atomic species that define the plane. Some lattice planes give rise to high-intensity diffraction and others weak diffraction.

BSE are electrons from the incident beam that exit the sample after one or more scatter events. A network of bands will be imaged on a phosphor screen (Fig. 1f), or EM film, located so as to intercept BSE (Venables and Harland 1973). The edges of the bands are conic sections of the two diffraction cones, associated with each lattice plane (Fig. 1f). One edge will be brighter than the other (Figs. 1c and 1d), reflecting the distribution of scattered electron intensities in relation to scatter angle (Fig. 1b). The Bragg angle for diffraction of electrons accelerated through a few tens or hundreds of keV is small (typically 0.5°), so that the opening angles of the diffraction cones are close to 180°. Thus the diffraction cones approximate planes, and the bands imaged appear straight sided (Figs. 1g and 1h). The bisector of each band is the direct projection of a lattice plane (Fig. 1f). Where diffractions of more than one order are significant, multiple bands will appear (Fig. 1g). These bands will share a bisector and will have width ratios corresponding to the ratio of the n values of diffraction order. For any lattice plane, the lowest-order diffraction allowable (depending on the space group) will have the highest intensity (Fig. 1g). Where bands intersect, they interfere positively. A large number of intersecting bands will give a bright spot on an EBSP (Fig. 1g) that corresponds to a zone axis. Bright zone axes are commonly surrounded by HOLZ rings (see Goodhew and Humphreys 1988; Fig. 1g). Intersections of a large number of bands may still give rise to bright spots even when the individual bands are not very intense (Fig. 1h). Symmetry elements can be defined, directly from the relative positions of bands and spots on an EBSP (Fig. 1h).

A model for beam-specimen interactions using only single-event elastic scattering is oversimplified. In general, incident electrons will penetrate into the specimen and will experience a series of elastic and inelastic scattering events until their energy is absorbed by the specimen or until they escape from the specimen (Fig. 2). There are two significant consequences for EBSD.

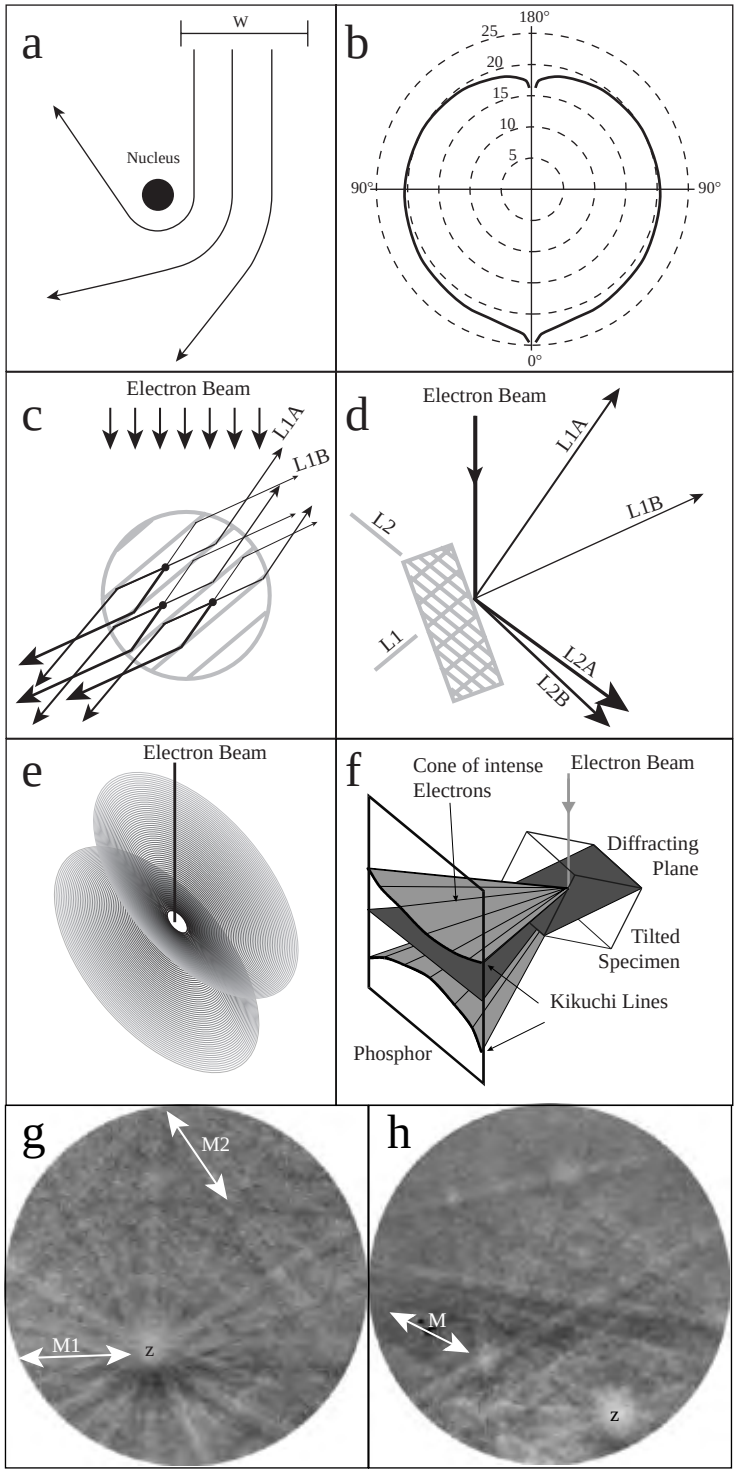

FIGURE 1. (**a**) Schematic illustration of the trajectories of elastically scattered electrons interacting with a single nucleus. W represents the width of the electron beam. Positions of the trajectories of individual electrons of the incident beam will be controlled by a probability function. Incident electron trajectories that pass close to a nucleus will be scattered through higher angles than those that pass more distantly. See Goldstein et al. (1992) and references therein for a more rigorous treatment. (**b**) Solid (onion shaped) line gives the magnitude of elastically scattered electron intensity as a function of scatter angle. Dashed circles provide a concentric scale showing scattering intensity, as log values of events/e^-/atom/cm^2, centring on the beam incidence point. Beam incidence is from top to bottom. Numbers in degrees show radial scatter angle. Calculations are made from equations for single scatter events (Goldstein et al. 1992: Equation 3.5) for an atomic number of 10 (Al: approximately the same as quartz). These calculations ignore diffraction effects. (**c**) Two-dimensional section through the beam-activation volume (schematic) with a single set of lattice planes that can give rise to diffraction. Elastically scattered electrons, with all possible trajectories are generated from all possible source points (three are shown) within the activation volume. Four scattered electron trajectories will satisfy the Bragg diffraction condition ($\sin\theta = n\lambda/2d$) for each of the source points. More than one order of diffraction (different values of n) will occur but are not shown on the Figure. The relative signal intensities of the 4 diffraction directions for each lattice plane, shown schematically by the thickness of the arrows, will vary as a function of the scattered electron intensity prior to diffraction (see 1b). (**d**) Two dimensional view of a sample with two sets of lattice planes that can give rise to diffraction. At the source point (point of beam incidence) there is an activation volume similar to that shown in 1c, except with two lattice planes. The activation volume is orders of magnitude smaller than the specimen. Lattice planes L1 are the same as those shown in 1c. Only diffracted rays L1A and L1B, from the four diffracted rays shown in 1c, escape as BSE. The other two rays penetrate into the sample. Two diffracted rays, L2A and L2B are associated with the second lattice plane L2. The relative signal intensities of the diffracted rays are shown schematically by the thickness of the arrows. (**e**) Schematic diagram showing single-order diffraction cones in three dimensions for a lattice plane (the lattice plane is not shown—it is the mirror plane that maps one cone onto the other). (**f**) Schematic diagram showing segment of single-order diffraction cones in three dimensions for a lattice plane within a sample (adapted from Day 1993). The diffraction cones can be detected by placing EM film or a phosphor screen in their path. The signal intensity of all diffracted trajectories is a function of the scattered electron intensity prior to diffraction (see 1b). One conic section imaged on the phosphor screen will be brighter than the other (unless the lattice plane contains the incident beam trajectory). Brightness will vary along the conic sections. (**g**) Example (background subtracted) EBSP from albite. The bisector of each visible band represents the projection, from the source point, of the lattice plane that gave rise to that diffraction band. At least three lattice planes have given diffractions of more than one order, visible as multiple bands (M1,M2). The prominent bright spot, formed at the intersection of a large number of visible bands (z), is the [001] zone axis; around this can be seen a HOLZ ring. (**h**) Example (background subtracted) EBSP from garnet. The prominent bright spot in the bottom right (z) is the <111> zone axis. None of the individual bands that cross to form the zone axis are particularly intense. There are, however, many of these bands so that the zone axis is bright. The {110} mirror plane (M) runs diagonally through the <111> zone axis.

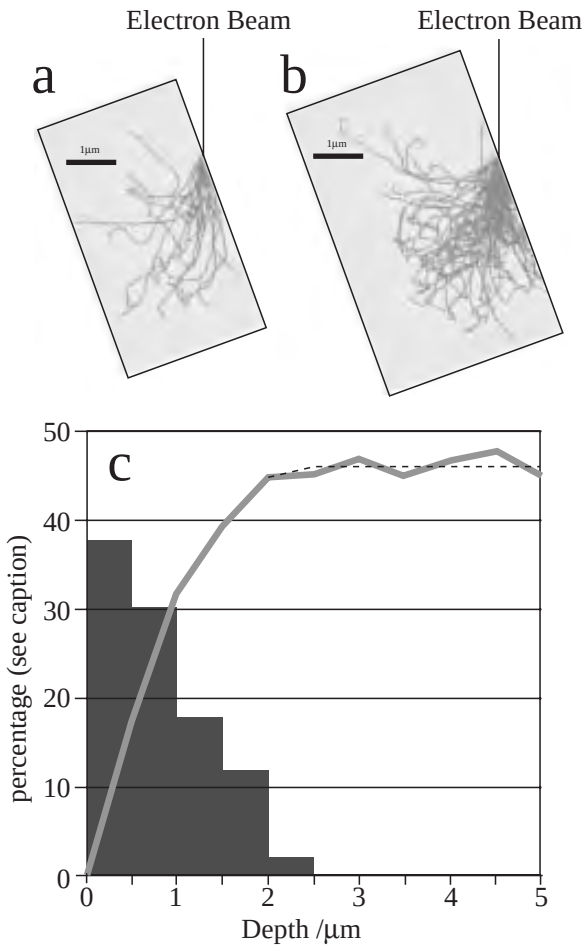

FIGURE 2. (**a**) Two-dimensional schematic illustration of the trajectories of electrons interacting with multiple nucleii in the plane perpendicular to the tilt axis. The figure shows the trajectories of 20 incident electrons modeled through the Monte-Carlo simulation in MATTER using plural scattering model for a sample of Al tilted at 70° to the incident beam using a 20 kV accelerating voltage. Scattering parallel to the tilt axis (perpendicular to the page) will be less intense than that shown. (**b**) Simulation as 2a, but showing the trajectories of 100 incident electrons. The simulation gives a good impression of the activation volume for BSE for an inclined specimen of Al. The activation volume is for all BSE of all energies. (**c**) Results of Monte-Carlo simulations (using plural scattering model in MATTER) to show BSE source depth for a sample of Al tilted at 70° to the incident beam using a 20 kV accelerating voltage. The solid line shows the percentage of incident electrons backscattered as a function of sample thickness. All electrons that are not backscattered are either transmitted or lose all their energy within the specimen. In each case, BSE were counted for 2000 incident electrons. The percentage of BSE is effectively constant at thicknesses >2–2.5 μm, suggesting that this is the maximum source depth although these BSE may span the whole range of energy between zero and the energy of the incident beam. The dashed line is a best-fit curve to the experimental results. This is used to calculate the percentage of total BSE from depth ranges 0–0.5 μm, 0.5–1 μm, etc, which are shown as gray columns.

(1) There will be a population of BSE and secondary electrons with energies between zero and E_0, the energy of the incident beam. Although the properties of the phosphor, together with potential for electron absorption, capture, and dispersion, will tend to eliminate signal related to lower energy electrons, the electrons that contribute to light emission from the phosphor will form a continuous polychromatic source. For any given *d*-spacing, the polychromatic electron energy corresponds to a continuous range of Bragg angles and gives rise to a diffuse background signal.

(2) The omni-directional source of scattered electrons from within the specimen is not a point but an activation volume. This will cause some blurring of the diffraction bands and it is the geometry of this volume that controls spatial resolution of the EBSD technique.

The size of the activation volume is critical to spatial resolution. Monte Carlo simulations (Fig. 2c) show that the maxi-

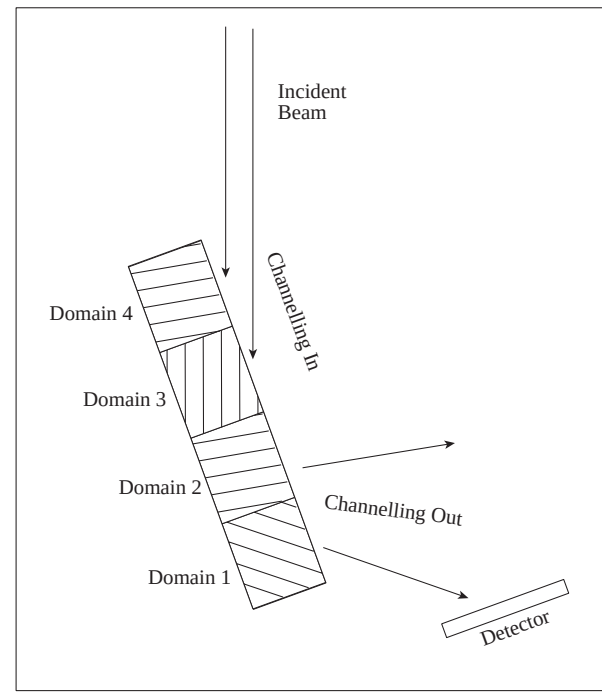

FIGURE 3. Schematic diagram to show how both channeling-in and channeling-out can give rise to OC images. The specimen is made of a series of orientation domains. The ruled lines in each domain represent, schematically, a strongly diffracting lattice plane. The channeling-out signal along the projection of this plane will be strong. The projection of the lattice plane of Domain 1 is intercepted by the detector, so that this will give a brighter signal than Domain 2, where the projection of the lattice plane is not intercepted by the detector. Channeling-in will cause differences in the penetration of the electron beam, and therefore of the resultant BSE intensity at the detector, for Domain 3, where the incident beam is oriented in the projection of the lattice plane and Domain 4 where it is not. In reality the processes are much more complex than this and are poorly understood. The figure has been drawn for an inclined specimen (as used in EBSD). Compare this with the normal scanning figure of Lloyd (1987).

mum source depth of BSE in aluminium (Al has an atomic number similar to the mean atomic number of many silicates) is 2–2.5 μm for typical EBSD working conditions (70° tilt and 20 kV accelerating voltage). Nearly 68% of total BSE are sourced from depths <1 μm. BSE exit the specimen surface up to 3.5 μm from the incidence point of the electron beam in the direction synthetic to the incident beam trajectory and perpendicular to the tilt axis, and 90% of all BSE exit within 2 μm of the incidence point along this same line. Electrons that penetrate more deeply into a specimen are more likely to have lost energy. Thus BSE that have energy close to E_0 are likely, on average, to be sourced more shallowly and exit closer to the incidence point than the Monte Carlo simulations predict for all BSE. Recent resolution tests (Humphreys et al. 1999), using a field-emission gun SEM (this gives a much smaller probe size for equivalent beam currents compared to a W filament gun), show that two EBSPs can be distinguished, separated by about 100 nm in the direction synthetic to the beam and from differently orientated Al grains. The same distinction can be made with only 30 nm separation in the direction parallel to the tilt axis, and resolution increases in materials with larger atomic numbers. It is likely that the sharp EBSPs are formed entirely from electrons that have experienced only one elastic interaction (low loss electrons), from within 10–20 nm of the specimen surface and with a width not much larger than the probe size (D. Dingley, personal communication). This would explain the disparity between activation volumes calculated from Monte Carlo simulations and observed resolutions. The quality of EBSPs depends upon the beam current. Larger beam currents give stronger signals but, through the electron optics of an SEM (Goldstein et al. 1992), also correspond to larger probe sizes and therefore reduced spatial resolution. There is always a trade-off between EBSP quality and spatial resolution.

The high resolution attainable in metals is not currently possible for non-conducting specimens, largely due to charging problems. Resolution on the order of 1 μm is possible using a tungsten filament and on the order of 0.25 μm using a field emmission gun (M. Drury, personal communication.).

ORIENTATION CONTRAST IMAGING

If an electron beam is scanned across the surface of a monomineralic sample and the BSE monitored with a solid-state detector in a fixed position, the BSE signal intensity will vary with the crystallographic orientation of domains within the sample. This effect is known as orientation contrast (OC), crystallographic contrast, or channeling contrast (Joy 1974; Lloyd 1987; Day 1993; Prior et al. 1996). The control of the lattice on the variation in BSE signal intensity with exit trajectory is known as channeling-out. The control of the lattice on the variation in BSE signal intensity with incident beam trajectory is known as channeling-in. OC can be understood in terms of both channeling-in and channeling-out (Fig. 3). There is good evidence that both channeling-in and channeling-out contribute to OC images, although the relative contribution from the two effects is unclear (Wilkinson and Hirsch 1997).

OC images can be collected in flat scanning, where the beam is subparallel to the normal to the specimen surface (Lloyd 1987), although the OC signal is an order-of-magnitude less than the signal related to Z-contrast between different minerals (Lloyd 1985, 1987). When the incident beam is at a high angle to the normal to the specimen surface, and solid-state detectors are positioned in the forward-scattering (Day 1993) or forescatter position (Prior et al. 1996), then the Z contrast is subordinate to the OC.

OC images are not quantitative (Joy 1974; Lloyd 1985; Day 1993, 1998; Prior et al. 1996; Trimby and Prior 1999; Day and Quested 1999). The signal intensity (gray scale) does not correspond to crystallographic orientation in a simple way so that: (1) two spatially distinct domains with different orientations can have the same signal intensities; (2) two spatially distinct domains with the same orientation can have different signal intensities; and (3) not all of the boundaries between differently oriented domains are visible.

To extract the most quantitative information from OC images, a series of images with different diffraction geometries are needed. Different diffraction geometries may be achieved by changing the trajectories of collected BSE (moving the detectors relative to the specimen), the trajectory of the incident beam (tilting or rotating the specimen), or the accelerating voltage (this changes the Bragg angles for all diffracting planes). Prior et al. (1996) showed that in a quartz mylonite one OC image may contain as little as 60% of the total domain boundary information and that six images of the same area, but with different diffraction geometries, are needed to define all the misorientation domain boundaries. Trimby (1998) suggested that the majority of domain boundaries that are invisible in individual OC images are low-angle boundaries. Day (1993, 1998) has developed a technique in which the images of a single specimen, collected from several differently positioned detectors, are combined digitally so that all of the misorientation domain boundaries seen in images from individual detectors are visible in one combined color orientation contrast image (COCI). In tests on metals (Day and Quested 1999), the COCI technique proves the fastest way to highlight all the misorientation boundaries in a specimen.

OC images comprise variations in gray scale (see examples later in this paper and in Lloyd 1987; Lloyd and Knipe 1992; Prior et al. 1996; Fliervoet 1995; McDonnell 1997; Trimby 1998; Trimby et al. 1998; Fliervoet et al. 1997, 1999; Boyle et al. 1998; Prior and Wheeler 1999; Trimby and Prior 1999). Sharp changes in gray scale usually correspond to a sharp change in crystallographic orientation (such as a grain boundary or sub-grain boundary) or structure (such as a phase boundary). Sharp changes can also correspond to channeling bands, particularly if the specimen contains large domains of a single orientation. Low-magnification forescatter OC images of single crystals always give a channeling pattern (Prior, unpublished experiments). If the specimen is moved by a translation then a misorientation/phase boundary will move (it may also change in intensity) whereas a channeling band will remain fixed. Small changes in accelerating voltage will cause a systematic translation of a channeling band but not of a misorientation/phase boundary. Gradual variations in gray scale usually correspond to gradual variations in crystallographic orientation. At low magnifications gradual changes may also reflect a change in channeling-in component as the beam orientation changes in a scan across an undistorted grain. In the latter case a translation

of the specimen will have no effect on the observed signal.

It is common to detect boundaries in OC images that have misorientation magnitudes (<0.5°) too small to be resolved from indexing EBSPs on either side of the boundary. The SEM can be used to image individual dislocations (Wilkinson et al. 1993) with lattice distortions of the order of 10^{-3} radians (0.06°). These studies attest to the view of the author that OC images can generally detect misorientations of low magnitudes (perhaps as small as 0.1°). Angular resolution is likely to depend on crystallographic orientation for any fixed beam-specimen-detector geometry. Rigorous comparisons of SEM and TEM microstructures are needed to assess better what the misorientation threshold is for OC images. Some preliminary observations by Trimby (1998) suggest that coating masks low misorientations and may be used as a control on misorientation threshold.

The spatial resolution of OC images will be controlled by activation volume considerations as outlined earlier and presented in Figure 2. In the case of EBSPs, the use of only the sharply defined diffraction pattern isolates a small activation volume associated with only the low-loss electrons (electrons with $0.99E_0$ or greater). This is considerably more difficult in the case of OC images, as semiconductor detectors without energy shielding image all electrons between their threshold energy (usually 2–10 keV) and E_0, so that the theoretical resolution is less than that of EBSD. In practice, domains on the order of 1 μm can be resolved with a W filament (Prior et al. 1996; Trimby et al. 1998; Trimby, 1998) and on the order of 0.25 μm with a thermionic field emission gun (McDonnell 1997; Fliervoet et al. 1999).

PRACTICAL USE OF ELECTRON BACKSCATTER DIFFRACTION

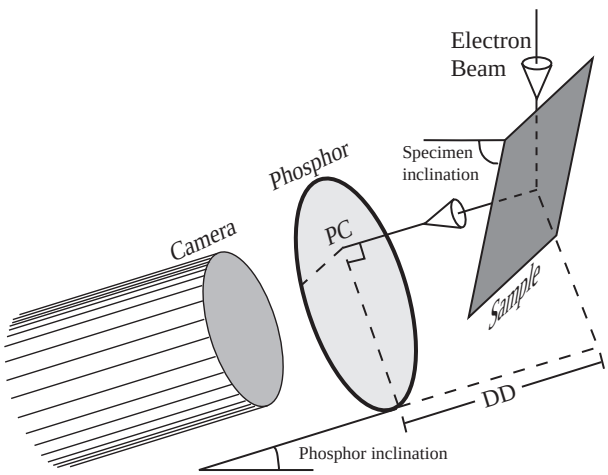

FIGURE 4. Typical hardware set up inside the SEM specimen chamber. For details of linkeage to software and processing see Dingley (1984), Wilkinson and Hirsch (1997) and Day and Quested (1999). Camera inclination and specimen inclination usually remain fixed for any hardware set up so that calibration requires deduction of the source point relative to the phosphor in terms of detector distance (DD) and pattern centre (PC). The specimen is viewed from behind.

DIFFRACTION

Specimen preparation for SEM-based crystallographic analyses

To access any crystallographic information using a SEM requires that a pristine crystalline lattice extends to within a few nanometers of the specimen surface. Crystal facets and fracture surfaces within crystals provide a pristine lattice but are not of general practical value. Mechanical polishing of blocks or thin sections damages the lattices of minerals at the specimen surface. Additional processes are required to remove the mechanical damage. Chemical-mechanical polishing (SYTON: Fynn and Powell 1979) provides a damage-free surface for most rock-forming minerals, although those that dissolve rapidly in the SYTON fluid (e.g., some micas, some potassium feldspars, and all hydrophylic clays) and some very soft minerals (such as galena) present preparation problems. Etching alone provides the damage-free surface required for EBSD, but the topography created makes EBSD work and OC imaging more difficult. Ion-beam milling is an unexplored alternative for removal of surface damage. This is likely to be slower and more expensive than SYTON and will be limited to the preparation of small surface areas (a few square millimeters), but may provide the only preparation technique suitable for some minerals. Samples must be kept scrupulously clean. Any dust particles will cast long shadows hiding local details of forescatter images and restricting EBSD analysis of those same areas. Specimen surface topography will have the same effect.

Experimental setup

To date, no SEMs have been built to optimize EBSD geometry. Thus, EBSD hardware configuration is restricted by existing chamber designs (Fig. 4).

The distance between the specimen and the phosphor screen is an important consideration in EBSD. The closer the phosphor is positioned to the source point the larger the angular range of the EBSP imaged (making indexing easier) and the better the signal detected on the phosphor screen. These advantages are balanced by the increased risk of physical interaction of the specimen and the phosphor, increased distortion of the EBSP in the gnomic projection (Randle 1992) and larger angular errors associated with source point position (see later). The requirement to position forescatter detectors (Prior et al. 1996) may also provide a constraint here.

Background subtraction

A live EBSP contains a significant background component related to the polychromatic source (Fig. 2c) and has an overall variation in signal intensity related to the variation of BSE electron intensities with scatter angle (Fig. 1b). The background can be isolated by assigning to each pixel the average signal for all pixels in a given diameter around that pixel (Fliervoet, personal communication) or collecting an EBSP with the beam scanning, or defocussed, over a large area so that the signal from a large number of crystals is averaged. If the crystals are of the same material they will have similar background signals and these will add constructively.

The first background isolation process is preferable as it enables the background for each individual analysis point to be assessed individually. The quality of an EBSP improves markedly after the backgound signal is subtracted from the total signal.

Calibration

Indexing an EBSP requires calculation of the solid angles between the planes that project as bands on the phosphor. The orientation of the phosphor and the specimen surface are usually pre-determined by the hardware or the user. The position of the source point relative to the phosphor is required and is usually expressed as the position of the pattern center (PC) and the detector distance (DD, Fig. 4). A number of methods of calibration have been tested (Randle 1992; Day 1993), however, it is common practice to calculate the PC and DD by collecting an EBSP of a known material (usually cleaved Si) in a known orientation.

Once an initial calibration is made, it is possible to refine the calibration parameters for any EBSP that can be indexed (Krieger-Lassen 1996). This process is particularly important as most hardware does not allow accurate repetition of standard and sample source points. There are errors involved in refinement and users should assess these for their system by making multiple calibrations and examining statistically the DD and PC data generated. The author (DJP) uses the average refinements of 10 distinct EBSPs after discarding the most extreme values from 12.

Indexing

Indexing is the process by which the EBSP of a known material is used to calculate the crystallographic orientation at the source point. The positions and orientations of bands are measured relative to the PC, either manually or using a Hough transform (Wright and Adams 1992; Wright et al. 1993; Schwarzer 1997; Krieger-Lassen 1998). Simple vector math can be used to calculate the orientations of the planes that contain bands and the source point. An algorithm can be used to calculate possible orientations of the crystal that give a match of these observed planes to a set of lattice planes of the material within given tolerances (Dingley 1989; Schmidt and Oleson 1989; Juul-Jensen and Schmidt 1990). Additionally, the bandwidths, which correspond to lattice plane *d*-spacings, can be incorporated into the algorithm. In order to apply indexing algorithms, the following information is needed about the material under analysis: (1) unit-cell lattice parameters, (2) crystal symmetry, and (3) a reflector file containing a list of the lattice planes that give rise to visible bands on EBSPs.

Items 1 and 2 are available for virtually all minerals, although the form of the data required depends on the indexing software. The third requirement is less trivial. There are an unlimited number of reflectors in a crystal structure, but using too many reflectors will slow-down processing and generate more incorrect solutions, whereas using too few may prevent the computer from finding any solution. A list of all reflectors in intensity order allows experimentation with different intensity cut-offs to optimize speed and precision of indexing. Kinematic models (Schmidt and Oleson 1989), based on atomic scattering factors together with site-occupancy data, provide good simulations for most minerals. Kinematic model reflector files for some minerals require minor modifications (e.g., quartz; N.H. Schmidt, personal communication). A few minerals are not characterized with sufficient precision by kinematic models (e.g., albite) and reflector files need to be developed by empirical means (Prior and Wheeler 1999). In the future, dynamic diffraction models may give better results in the simulation of EBSPs.

Assessment of whether the computer has indexed a pattern correctly requires comparison of the observed EBSP with a simulation (usually overlayed on the EBSP). A good fit requires that all the visible bands are simulated and that there are no bands in the simulation that are not observed. Each new mineral will require some experimentation to find a reflector file that simulates the EBSPs correctly. This may require calibration with crystals cut in known orientations (Lloyd and Ferguson 1986; Prior and Wheeler 1999). At the time of writing, computer algorithms are still incapable of consistent, first-time, correct indexing of many of the important rock forming minerals (Fliervoet et al. 1999; Prior and Wheeler 1999). In both quartz and plagioclase, for example, 20–30% of first solutions are incorrect and a human operator is needed to detect and correct these mistakes.

The magnitude of misorientation on individual boundaries, calculated from two indexed EBSPs, has an error of ~0.5° for manual identifcation of bands and ~0.75° for bands picked using a Hough transform (Krieger-Lassen 1996). Absolute orientations, relative to geographic space for example, will comprise these errors plus any errors associated with positioning the specimen. The errors on misorientation axes calculated from EBSD data decrease as misorientation magnitude increases (Prior 1999). For misorientation magnitudes of ≥20°, individual measurements of misorientation axes will be within 5° of the true value (Prior 1999). Where appropriate, misorientation axes can be defined on the basis of the distributions of individual measurements. For misorientations of ≥10°, 30 data points should suffice, but more data are needed for smaller misorientations (Prior 1999). Individual misorientation measurements of low-angle boundaries need to be treated with caution. Wilkinson (1996, 1997) has developed high-precision techniques for measurement of angular changes as small as 0.01°, and adoption of similar techniques is required for detailed analysis of small misorientations.

Locating analysis points

Analysis points, unless being collected on a line or grid, as in automated EBSD (see next section), need to be located using an image. Depending on circumstances, the image used may be an OC or COCI image using forescatter detectors, a Z-contrast BSE image, or a secondary electron image. Where EBSD data are to be linked to an imaged microstructure, it is worth collecting high-quality images in advance of analysis. Both OC and Z-contrast images can be collected with better quality in the absence of the restrictions of the EBSD phosphor (Prior et al. 1996).

If EBSD data of highest quality are required, then it is important that the specimen be moved to a fixed analysis point.

To locate points without moving the specimen changes the beam trajectory and thus the source point. The errors involved in doing this are presented in Figure 5. The misorientation axis would be affected much more significantly by the same source point errors (Prior 1999). Change of source point, associated with beam movement, also can be corrected by changing calibration parameters dynamically.

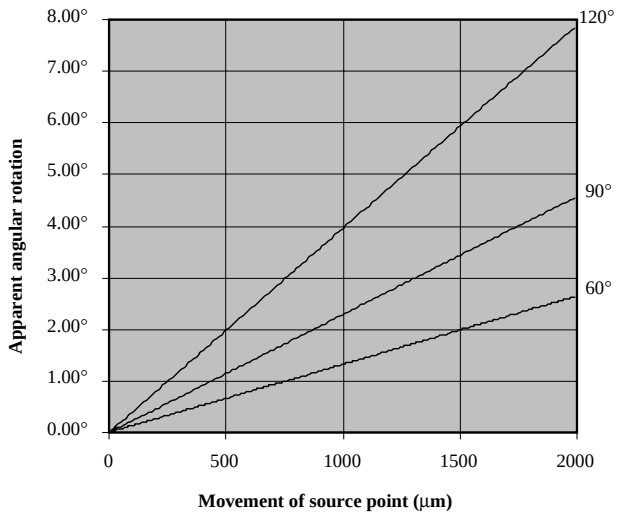

FIGURE 5. Estimate of errors involved in moving the source point (moving the beam) during analysis. Errors are expressed as an apparent angular rotation (δ) and are calculated using the approximation $\tan \delta = d/DD$, where d is the distance the source point has moved. Calculations are made for three DDs of 14.3, 25, and 14 mm, which correspond (for a 50 mm phosphor) to opening angles of the imaged EBSP of 120°, 90°, and 60° respectively. Opening angles for the three data sets are shown on the right hand side of the figure.

Fully automated EBSD: orientation mapping

Computerized band recognition, indexing, and SEM control (Juul Jensen and Schmidt 1990; Krieger-Lassen et al. 1992; Adams et al. 1992; Wright and Adams 1992; Wright et al. 1993; Humphreys 1999) have led to fully automated EBSD systems. These systems can collect and index a pattern, store the data and move the beam/stage to another analysis point in times of the order of 0.2 s. Data can be collected at predefined points, on transects, or on a grid. Grid data are used to reconstruct the microstructure of the specimen (Fig. 6). Reconstruction can be made by coloring pixels on the basis of a look-up table (based on euler angles, pole figures, or inverse pole figures, for example) or by picking changes in orientation to define boundaries (with >10° misorientation for example).

In applying orientation mapping to rocks, charging and specimen preparation problems mean that many points give poor pattern quality so that a reconstruction of the microstructure will be a slave to the algorithm that fills these points that contain no data. Minerals that have severe mis-indexing problems require manual intervention for a high proportion of data points and cannot easily be treated by automated EBSD. In the Earth sciences, the application of automated EBSD procedures and orientation mapping has been limited by these problems. However, significant progress has been made in experiments in a number of laboratories (Trimby, personal communication; Lloyd, personal communication; Kunze, personal communication) and first results should be published over the next few years. Particular success has been achieved in automated analysis of calcite (McCaig and Lloyd, Kunze, work in progress) rock salt (Trimby et al., work in progress), and FeTi oxides (Trimby, work in progress). Alternative approaches using OC or COCI images to find orientation domain centroids and collecting one EBSP per orientation domain (Day and Quested 1999) may provide a more-plausible automated mapping procedure for those minerals with severe mis-indexing problems and for samples with severe charging problems.

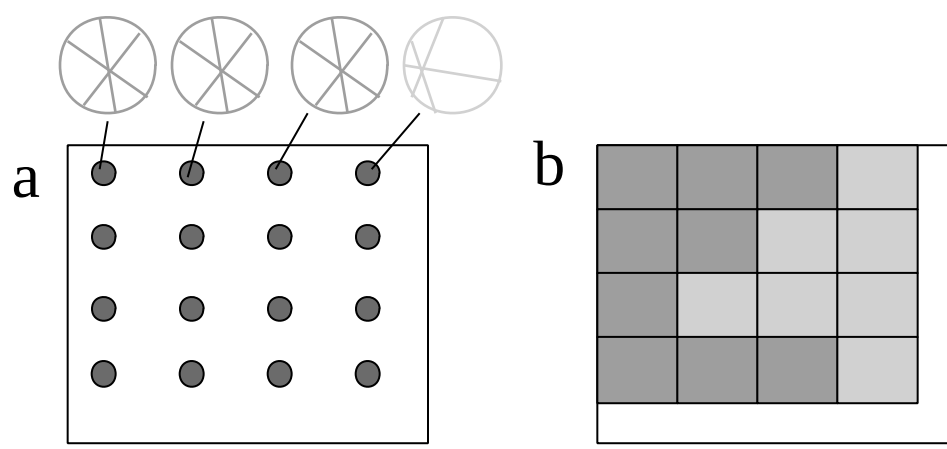

FIGURE 6. Schematic illustration of orientation imaging. EBSPs are collected at a grid of stations: (**a**) polygonal area around each sample station is assigned the orientation at that station and (**b**) these polygons can be colored to show the orientation (see text).

Charging

Insulating specimens will experience charge build-up under an electron beam. Charging remains a rather unpredictable and specimen dependent problem. In the worst cases, it can prevent meaningful EBSD work; in other cases, uncoated specimens can be examined with few problems. Typical charging problems are outlined in Goldstein et al. (1992). Coating the specimen with a conductive material such as carbon or gold removes the problem of charge build-up, but reduces the quality of EBSPs and OC images. EBSP quality can be increased by raising beam current, and concomitant probe diameter. EBSPs from specimens with 4–6 nm of carbon coat require one or two orders of magnitude more beam current than that required to generate EBSPs of equivalent quality in uncoated specimens (Prior, unpublished experiments). Thus, coating requires an increased spot size and a reduced spatial resolution for EBSD work. OC images from uncoated specimens are always of much higher quality than those from coated specimens.

THE DATA THAT CAN BE COLLECTED

An EBSP provides the full crystallographic orientation of a point (<1 μm) in a specimen. In order to use the data, it is crucial that the angular relationships between the specimen-surface and microscope reference frames are known. Knowledge of the relationships between the specimen-surface reference frame and any appropriate kinematic reference frame (foliation, lineation, and shear sense) enables fuller interpretation of the data (Passchier and Trouw 1996), and knowledge of the angular relationships between specimen-surface and geographic reference frames enable regional analysis. EBSD data can be collected from a grid of points, line transects of points, randomly located points, or a point in every orientation domain identified in a specified area. From these data one can examine the distributions of individual orientation measurements related to the microstructure (microtexture), the statistical distributions of orientations (the average texture of a bulk sample: macrotexture), and the misorientations between individual measurements (mesotexture). The terms in parentheses are those adopted in material sciences (see Randle 1992).

Orientation distributions

The data set of orientation measurements comprises a measure of the crystallographic preferred orientation (CPO: also known as the lattice preferred orientation or, in materials and metallurgy literature, the texture or macrotexture) of a specimen. Data display of CPOs from EBSD data is reviewed by Randle and Caul (1996).

CPOs are commonly displayed as pole figures, in which poles to lattice planes, or zone axes, are plotted on a stereonet relative to specimen reference orientations. An alternative representation is the inverse pole figure, in which a specimen reference orientation (such as a lineation or pole to foliation) is plotted relative to crystallographic reference axes, in the primitive symmetrical unit for the mineral concerned.

Pole figures and inverse pole figures are easy to understand but have a disadvantage in that at least two points have to be plotted in order to describe fully one measurement of orientation. Orientation distribution function (ODF) techniques (Bunge 1982; Schmid et al. 1981) enable representation of individual crystallographic orientations as single points. Various ways of representing ODFs are reviewed by Randle and Caul (1996) and Wenk and Kocks (1987). Randle and Caul (1996) review representations of EBSD data.

The spatial variation of orientations can be displayed, simply by coloring the individual orientation measurements according to a defined look-up table. The look-up table may be created from a pole figure, inverse pole figure, or ODF, or may correspond to numerical values of Euler angles or ideal orientations (see Randle 1992). This approach was developed by Sander (1930, 1970), who called the figures "Achsenverteilungsanalysen" or AVA diagrams.

Misorientation distributions

Since each EBSP provides the full crystallographic orientation of a point, the rotation required to map the orientation at one point onto the orientation at another point can be calculated. This rotation can be represented in a number of ways (Randle 1992) but it is becoming conventional to refer to the angle and axis of the rotation. The number of possible misorientation angle-axis pairs that can be calculated from two indexed EBSPs depends on the mineral symmetry. In triclinic crystals there is only one solution whereas in trigonal crystals (e.g., quartz) six and in cubic crystals (e.g., garnet) 24.

The misorientation axes and angles are usually represented in separate diagrams. The frequency, or the cumulative line-length, of boundaries, between neighboring grains, with given mismatches are plotted (Lloyd et al. 1997; Trimby et al. 1998; Fliervoet et al. 1997; 1999). This is known as the correlated misorientation distribution. Another approach is to find the mismatch between every measurement and every other measurement in a population, or between randomly selected non-neighbor pairs. This is known as the uncorrelated misorientation distribution and gives a measure of the expected misorientation distribution, as a function of the CPO (Humphreys and Hatherley 1995; Fliervoet et al. 1999). In the case of non-triclinic minerals, the smallest of all the symmetrically equivalent misorientation magnitudes is used to generate the magnitude distributions. The consequences of this assumption have not been fully explored. Misorientation axes are plotted, most usefully, on inverse pole figures (Trimby 1998; Fliervoet et al. 1999; Faul and FitzGerald 1999), as all the symmetrical equivalents will plot in the same place.

There are methods, most notably the use of Rodrigues-Frank vector space (Frank 1988; Day 1993; Randle 1992; Randle and Caul 1996) and misorientation distribution functions (MODFs) analagous to ODFs for orientations (Pospiech et al. 1986; Schwarzer and Weiland 1988), that enable direct plotting of axis-angle pairs. These approaches are, as yet, little explored in the Earth sciences.

The spatial variation of misorientation magnitudes or misorientation axis orientations can be displayed, simply by coloring the boundaries according to a look-up table of misorientation magnitudes, misorientation axis orientations, or MODF parameters.

The geometry of grain/phase boundaries

There is a concept that the energy associated with any boundary in monomineralic materials is related to the geometry of

that boundary (Humphreys and Hatherley 1995). Low-angle tilt boundaries have relatively low energies, which increase with crystallographic misorientation. Non-tilt boundaries will have higher energies, although the energies of boundaries with coincidence site lattice (CSL) geometries (op cit) will be lower. The bulk physical properties of a material can be influenced by the boundary network, as the processes at each individual boundary are controlled by its properties (op cit). Although the detailed structure of grain boundaries, imaged by TEM, has been a focus of investigations in Earth sciences (e.g., McClaren 1986), the relationships between boundary structure and geometry have received less attention. Spry (1969) emphasized the importance of boundary geometry, particularly misorientations, but little further development has been made, largely due to the difficulties in measuring misorientations. Selected area electron channeling patterns (SAECP) provided the first practical way of measuring the geometry of a large number of boundaries (Farmer 1992; Lloyd et al. 1997). SAECP is largely superceded by EBSD techniques, which have better spatial resolution and are faster and easier to apply, although angular resolution is poorer. EBSD does not provide all of the information required to quantify fully boundary misorientations, because the orientation of the boundary plane remains unknown. The trace of the boundary can be measured from OC images or the results of orientation mapping, but its 3-D orientation requires it to be visible on two differently oriented surfaces (Randle and Dingley 1989) or to be constrained at two depths by serial grinding (Randle 1995)

PRESENT AND POTENTIAL FUTURE APPLICATIONS IN PETROLOGY

Phase identification

EBSD and orientation mapping are now used as standard techniques for phase discrimination in metals (Field 1997; Randle 1994). There is clear potential to use EBSD as a tool for discrimination of mineral polymorphs. Preliminary studies show that EBSD can be used to distinguish microcrystalline (<10 μm) andalusite, sillimanite, and kyanite (Prior and Spiess, unpublished experiments) and quartz and coesite (Prior et al., unpublished experiments).

Some high *P-T* phases, such as α-quartz, are predicted to be important in metamorphic rocks but are never preserved because transformations to lower *P-T* phases (β-quartz) are diffusionless and instantaneous. Other high *P-T* phases may be important during the high *P-T* history of the rock but may not survive the later rock history. Detailed microstructural studies using EBSD provide the potential to infer the previous activity of phases that are no longer present in a rock. Randle and Caul (1996) demonstrate that the frequency of misorientation magnitudes in α-titanium is consistent with its formation by a transformation from β-titanium. Kruhl (1996) distinguished subgrain microstructures that formed during the stability of α-quartz and β-quartz. Dauphiné twin boundaries, which form as a geometrical requirement of the α-quartz to β-quartz transformation, are easily recognizable using EBSD data (Trimby et al. 1998; Trimby 1998). Coupling Dauphiné twin-boundary frequency with other microstructural criteria should provide an improved tool to establish in which stability field deformation, recovery, and recrystallization occurred. Understanding the microstructural effects of the α-quartz to β-quartz transformation is of particular significance given that experimental deformation of quartz, by necessity (E.H. Rutter, personal communication), is conducted in the stability field of α-quartz whereas natural deformation occurs mainly in the stability field of β-quartz. Similar microstructural tools may be developed to establish stability fields of deformation for other systems such as calcite-aragonite and olivine-spinel. Indeed, Lloyd (personal communication) has made significant progress in demonstrating that olivine CPOs of mantle nodules are consistent with slip systems that occur in the spinel structure but not in the olivine structure.

Constraints on deformation mechanisms:

The mechanisms controlling deformation during laboratory experiments can be constrained from constitutive relationships of stress, strain rate, temperature, and grain size (Frost and Ashby 1982; Green 1998). The microstructures resulting from such experiments can be examined (e.g., Hirth and Tullis 1992; Rutter 1995) and correlated to the dominant processes. Thus, empirical links between natural and experimental microstructures, as described later, provide constraints on dominant deformation mechanisms in natural rocks. However, problems of extrapolation of data from experimental to natural conditions, and the likelihood that more than one mechanism may be operating (although only one dominates the rheology) necessitate independent methods of assessing the mechanisms in natural and experimental samples. In addition, the balance of processes such as recovery and different recrystallization mechanisms may modify material behavior without giving rise to an identifiable signal in the constitutive relationships. The identification of different recovery and recrystallization mechanisms (Hirth and Tullis 1992) through studies of microstructure thus becomes crucial to studies of experimental and natural samples alike.

The form of CPOs has been used as a constraint on deformation processes for almost a century (see review in Wenk and Christie 1991). In rocks deformed in the solid-state, the absence of a CPO indicates deformation by a mechanism that is not controlled by mineral crystallography, such as frictional or diffusion-accommodated grain-boundary sliding. In contrast, the presence of a CPO is commonly related to operation of deformation mechanisms with a crystallographic control, namely dislocation creep or twinning (Wenk and Christie 1991; Passchier and Trouw 1996). One must be careful in the interpretation of such data, as different mechanisms can be dominant on different scales. For example, Boyle et al. (1998) showed that individual pyrite grains in a deformed ore have microstructures and intragrain CPOs consistent with a dislocation creep mechanism in the same sample in which the macrotexture of hundreds of pyrite grains is random. Such observations emphasize the importance of the extra information gained in the microtextural approach, in which orientation measurements are clearly linked to the microstructure. Microtextural studies using SAECP (Lloyd et al. 1987, 1991, 1992, 1997; Lloyd and Freeman 1991, 1994) and optical studies linked to X-ray texture goniometry (Law 1987, 1990; Law et al. 1986, 1990) have greatly increased our understanding of deformation mechanisms. CPOs that relate to specific microstructural environments

can be identified and misorientation data can be calculated. Such data are now collected more easily and quickly with EBSD coupled to OC images (Trimby et al. 1998; Trimby 1998; Boyle et al. 1998; Fliervoet et al. 1999; Prior and Wheeler 1999).

Quantitative data from EBSD and OC imaging enable rigorous testing of deformation models using statistically representative data sets. An example is the application of boundary hierarchies (Trimby et al. 1998). Conceptual models suggest that the processes of recovery, subgrain rotation and grain-boundary migration recrystallization each produce identifiable boundary hierarchy signatures during dislocation creep deformation (Trimby et al. 1998; Trimby 1998). Figure 7a shows two boundary hierarchy data sets for a quartz mylonite (Trimby et al. 1998). Hierarchy A is consistent with the operation of recovery and subgrain rotation (Figs. 7c–7k) and was quenched before achieving a steady state (Means 1981). Hierarchy B is more difficult to explain, although it is not consistent with subgrain rotation alone or grain boundary migration alone, rather with some dynamic balance of both processes that achieves a steady state.

Modeling of microstructural processes (e.g., Etchecopar 1977; Lister et al. 1978; Jessell 1988; Nichols et al. 1991; Humphreys 1997; Campbell et al. 1998), with the aim of predicting the whole range of parameters measurable using EBSD and OC techniques, is an important research area for the future, which should enable a much more rigorous linkage of microstructural observations to deformation mechanisms (Trimby et al. 1998)

Constraints on dislocation slip systems

Slip systems of individual dislocations are calculated from TEM observations (McClaren 1991). Direct observations of dislocations in the SEM (Wilkinson et al. 1993) may, in the future, be applicable to single-crystal specimens of rock-forming minerals. At present, we must rely on the misorientation geometry, which relates to the slip systems of deformation in materials that have deformed by dislocation creep. A simple model constrains both the slip vector and the pole to the slip plane of the slip system associated with subgrain boundaries to lie in the plane perpendicular to the observed rotation axis (Lloyd et al. 1997; Boyle et al. 1998).

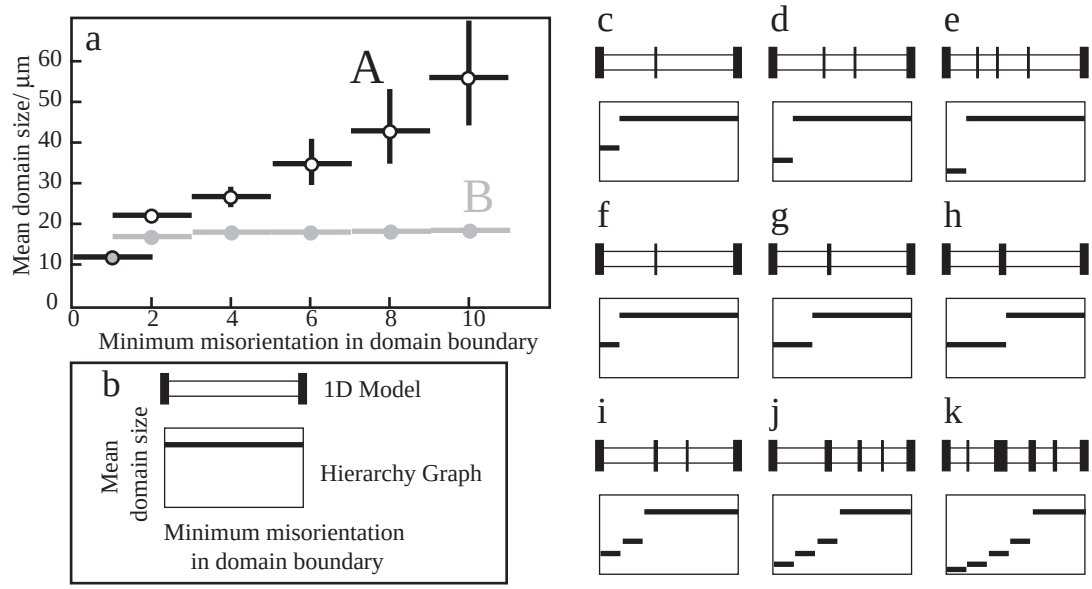

FIGURE 7. (**a**) Two boundary hierarchies from a quartz mylonite (Trimby et al. 1998). To measure the data point corresponding to a given minimum mismatch, a map is drawn of all boundaries with that mismatch (or greater). The size of each individual enclosed cell defined in the map is measured and the mean of these data plotted as the domain size for that minimum mismatch. Hierarchy A can be explained by recovery and subgrain rotation processes (see 7b–k). Dots are average data, lines represent standard deviations. (**b**) Starting configuration of conceptual model used in 7c–k. Upper part of diagram shows a 1D grain bound by two boundaries with >10° misorientation. All maps drawn (for ≥1° mismatch or ≥5° mismatch, for example) will define a single domain size equal to that for ≥10° mismatch. (**c**) Recovery to form a single subgrain boundary of small mismatch will define a domain size half the starting domain size for all mismatches up to the mismatch of the subgrain boundary. All higher mismatches will define the starting domain size (see 7b). (**d**) Further recovery to form a second subgrain boundary will reduce the domain size for all mismatches up to the mismatch of the subgrain boundaries to 1/3 the starting domain size (see 7b). (**e**) Further recovery to form a third subgrain boundary will reduce the domain size for all mismatches up to the mismatch of the subgrain boundaries to 1/4 the starting domain size (see 7b). (**f**) same as 7c. (**g**) Rotation of the subgrain boundary to increase its mismatch will cause the step between the two domain sizes set up by initial recovery (Fig. 7f) to move to higher mismatch values. (**h**) Similar to 7g, but more evolved. (**i**) After the stage seen in 7g, further recovery causes development of a new subgrain boundary and three distinct domain sizes will be established. (**j**) Effect of subgrain rotation increasing the misorientation of all the subgrain boundaries in 7i and further recovery causing development of a new subgrain boundary. (**k**) Effect of subgrain rotation increasing the misorientation of all the subgrain boundaries in 7j and further recovery causing development of a new subgrain boundary. The stepwise hierarchy developed by the combined operation of recovery and subgrain rotation is very similar to observed hierarchy A in 7a.

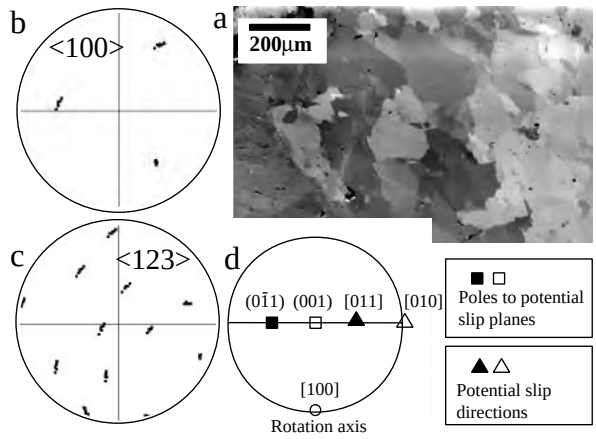

FIGURE 8. (**a**) OC image showing the microstructure of garnet from an alpine eclogite. Everything, except the extreme left of the view is garnet. (**b**) Plots of <100> axes from a left to right transect of EBSD analyses across the OC image shown in 8a. The upper two concentrations show a dispersion whereas the bottom right <100> axis is tightly clustered, suggesting that the data represent a rotation of orientations around the clustered <100>. (**b**) Plots of {123} poles from a left-to-right transect of EBSD analyses across the OC image shown in 8a. These data emphasize that individual poles lie on small circles around the bottom right <100> axis in 8b. (**c**) Stereonet to show two possible slip systems that could explain rotation around a <100> axis. Solid symbols show (0$\bar{1}$1)[011] and open symbols (001)[010]. We cannot distinguish the symmetric equivalents in {110}<110> and {100}<100> and only one set is shown for clarity.

Further technical developments are required before misorientation axis measurements across individual low-angle boundaries have sufficient precision to constrain slip systems (Prior 1999). However, dispersions of orientations across a number of boundaries can often reveal the boundary misorientation geometries, overcoming the imprecisions in individual measurements (Prior 1999). EBSD collected across deformation substructures in some cases show small circle dispersions around a rational crystallographic zone axis. An example data set from a deformed garnet is shown in Figure 8. Measurements across a set of orientation domain boundaries, located using an OC image, show that the subdomains are progressively misoriented by rotation around one of the garnet <100> axes. Individual misorientations are small (generally < 2°) although the misorientation across the entire data set is about 9°. These data lead to the interpretation that the sub-domain boundaries are crystallographically controlled and are likely to be subgrain boundaries. In this case {001}<001> or {110}<110> are possible garnet slip systems (Fig. 8d). Similar observations have been made for pyrite (Fig. 9b), where the rotation axes are parallel to <100> and <110> (Boyle et al. 1998) and for dolomite, where clear rotation axes are parallel to <11$\bar{2}$0> and less-defined rotation axes parallel {10$\bar{1}$4}, {01$\bar{1}$2}, and [0001] (Leiss and Barber 1999).

Comparison of observed CPO data with experimental results, simple kinematic models, and more-sophisticated dynamical models are used to constrain which slip systems have been important in the deformation (e.g., Schmid and Casey 1986; Law et al. 1990). Bulk-data misorientation distributions also

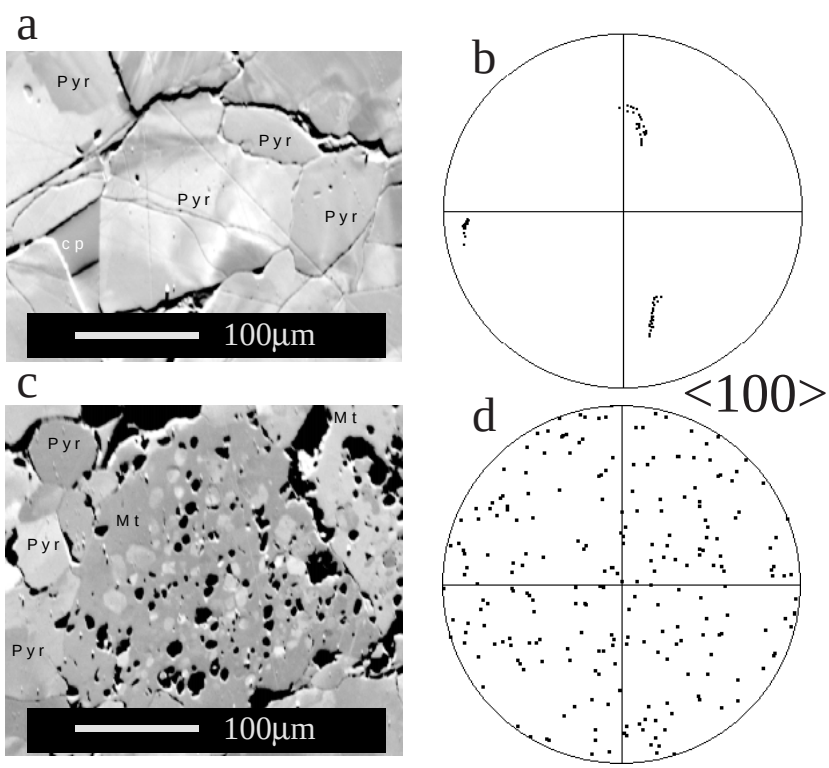

FIGURE 9. (**a**) OC image of plastically deformed pyrite porphyroblasts from the Sulitjelma ore body, Norway (Cook et al. 1993). Pyr = pyrite. Cp = chalcopyrite. (**b**) Plot of <100> axes across the deformed pyrite porphyroblast shown in 9a, showing dispersion of data corresponding mainly to a rotation around the left hand <100>. (**c**) OC image of magnetite grain of similar size to the pyrite in a. The magnetite (Mt) has inclusions of pyrite with many different shades of gray. (**d**) Plot of <100> axes of pyrite inclusions in the magnetite shown in Figure 10c. These are random and are unlike the pattern observed in single pyrite porphyroblasts (Fig. 9b).

can show rotation axis trends and can constrain slip systems in large data sets (Farmer 1992; Lloyd et al. 1997). Misorientation data have yet to be compared to deformation models in the same way that CPO data are.

Empirical quantification of deformation microstructures

Empirical links can be used to correlate measurable microstructural parameters to deformation conditions. The best example of this is palaeopiezometry. For dislocation creep deformation, measured parameters such as grain size, subgrain size, or dislocation density are linked to flow stress magnitude via a model (Twiss 1977; 1986) or experimental calibration (Koch 1983; Mercier et al. 1977). These approaches ultimately are dependent on how rigorously microstructural parameters can be defined. In the case of grain size and subgrain size palaeopiezometry, there has been a problem of what is meant by "grain" or "subgrain." Imprecision in the definition of these parameters must lead to significant errors in the application of these methods. If sizes are calibrated experimentally, then it must be clear that the same parameters are measured by the same methods and at the same scale in both the calibration experiments and in the samples. If measurements are to be compared to models, then the model must yield a parameter that is measurable in the sample. Measured parameters for calcite twinning palaeopiezometers (Rowe and Rutter 1990) are defined rigorously, which, in part, explains the better precision of calcite twinning palaeopiezometers compared to grain and subgrain size palaeopiezometers. The boundary hierarchies approach (Trimby et al. 1998) provides a much more rigorous, objective way of comparing domain sizes in natural (Fig. 7a) and experimental samples and may be the basis for a much better "grain size" palaeopiezometer. A pilot study (Trimby 1998) has attempted to apply the boundary hierarchies technique to experimental samples from Hirth and Tullis (1992). The pilot study showed that the extremely fine-grained nature of some experimental charges excludes them from detailed EBSD studies until charging problems are overcome. However, samples from regime 3 of Hirth and Tullis (1992) yielded full hierarchy data and a pattern that is very similar to natural mylonites.

The approach adopted most widely to constrain deformation conditions is the construction and use of deformation mechanism maps (Ashby 1972; Frost and Ashby 1982; Passchier and Trouw 1996). In this approach, the results of laboratory deformation experiments are used to constrain boundaries between regions of temperature-stress-strain rate-grain size (pressure, fluid activity, etc.) space in which particular deformation mechanisms dominate. The microstructure of natural samples are used to infer the dominant mechanism active during deformation and comparison with the deformation mechanism map enables constraint of the range of conditions that must have applied. The approach has the weakness that the user must interpret the sample mechanisms before consulting the mechanism map. Because there may be disagreement as to what sample microstructures correspond to what mechanisms, problems arise. As most modern experimental studies present rheological data and the resultant microstructures (e.g., Hirth and Tullis 1992; Rutter 1995, 1998), it would seem more appropriate to compare, quantitative microstructural parameters directly to produce characteristic microstructure maps (CMMs) as an alternative and an accompaniment to deformation mechanism maps. CMMs would have the advantage of being sensitive to gradual changes within one mechanism field and the operation of more than one mechanism. The approach could also take into account the effects of strain on the specimen microstructure (Rutter 1998; Trimby et al. 1998) and that microstructures may be modified constantly on some deformation *P-T-t* path (Knipe 1989; Prior et al. 1990). Boundary hierarchies (Trimby et al. 1998), quantitative misorientation statistics (Fliervoet et al. 1999), and boundary topology (Kruhl and Nega 1996; Takahashi et al. 1998; Tanaka et al. 1998) all represent rigorous, repeatable methods that could be applied to both experimental and natural samples to constrain CMMs. The data set could be extended by using natural samples, with independently constrained deformation conditions (from metamorphic data for example) as reference points (cf., McClay and Ellis 1983; Kruhl 1996). EBSD and OC techniques are being applied widely to experimental samples (Fliervoet et al. 1999; McDonnell 1997; Trimby 1998) and represent the best way of linking experimental and natural samples empirically.

Constraints on metamorphic processes

The geometry of boundaries between phases has received less attention than the geometry of boundaries in monomineralic aggregates. Studies of metamorphic reactions using TEM (e.g., Brearley 1987; Worden et al. 1987, 1991) have shown that nucleation and growth of new phases can be strongly controlled by crystallographic orientation and that these data have considerable importance in understanding phase transformation mechanisms (Brealey 1987; Worden et al. 1987, 1991; Brearley et al. 1992; Rubie and Brearley 1994; Putnis 1992). Common observations such as mimetic overgrowths (Spry 1969), development of specific orientations in exsolution (Pryer et al. 1995), and oriented symplectites indicate that there must be some combination of nucleation site orientation and interface control on metamorphic reactions. In addition, grain-boundary properties will influence grain-boundary diffusion, which is important in metamorphic and deformation processes (Wheeler 1987, 1991, 1992). Thus it seems odd that metamorphic petrologists have not been forward in demanding more representative crystallographic tools as offered by the SEM. Some studies of metamorphic problems have used the SAECP technique (Lloyd et al. 1991; Prior 1992; Pryer et al. 1995), but more extensive studies have been limited by the difficulty of gathering OC images and SAECPs when Z-contrast is the dominant image component (Prior et al. 1996). These problems do not arise in collection of EBSD data and OC images using forescatter detectors. Some examples will be used to illustrate the power of the EBSD technique in providing data pertinent to metamorphic problems. The data shown here are in opaque and isotropic phases for which observations of substructure have previously been very difficult.

Samples of deformed, amphibolite facies, massive sulfide ore from Sulitjelma, Norway (Boyle et al. 1994; Cook et al. 1993) have been studied extensively using OC images and EBSD (Boyle et al. 1998). The dominant opaque minerals are pyrite porphyroblasts, with subordinate matrix chalcopyrite and sphaler-

ite. Magnetite crystals with abundant small (<10 μm) pyrite inclusions occur in some ores, apparently as a replacement product of pyrite porphyroblasts (Fig. 9c). EBSD measurements show that the pyrite inclusions are randomnly oriented (Fig. 9d). Pyrite porphyroblasts (150–600 μm), not included in magnetite, show substructure (Fig. 9a), but the misorientations across internal boundaries are small, and the cumulative misorientation within each porphyroblast is systematic and typically <20° (Fig. 9b). The inclusion orientations cannot represent simple relics of the orientations in an original pyrite replaced by magnetite, and new models need to be sought to explain the texture. A model of channelized flow of oxidizing fluids resulting in localized brittle hydraulic fracture of pyrite and replacment of shocked pyrite by magnetite is under investigation (Boyle et al., work in progress)

Clusters of many hundreds of garnets, as small as 5 μm, form millimeter-sized garnet rich ellipsoids in schists from the Northern Italian Alps. Work in progress (Spiess et al.) aims to constrain the nucleation and growth processes that control the development of the garnet clusters. The clusters comprise individual small garnets (<50 μm), some individual large garnets (typically >200 μm) and garnets that contain sub-domains with different orientations, such as the garnet shown in Figure 10a. An interpretative model to explain such sub-domains is that the garnets nucleated separately but have amalgamated during growth (Fig. 10b). Some larger areas show a much more complex substructure (Fig. 10d). In detail the contacts between different sub-domains show faceted forms and an overall geometry

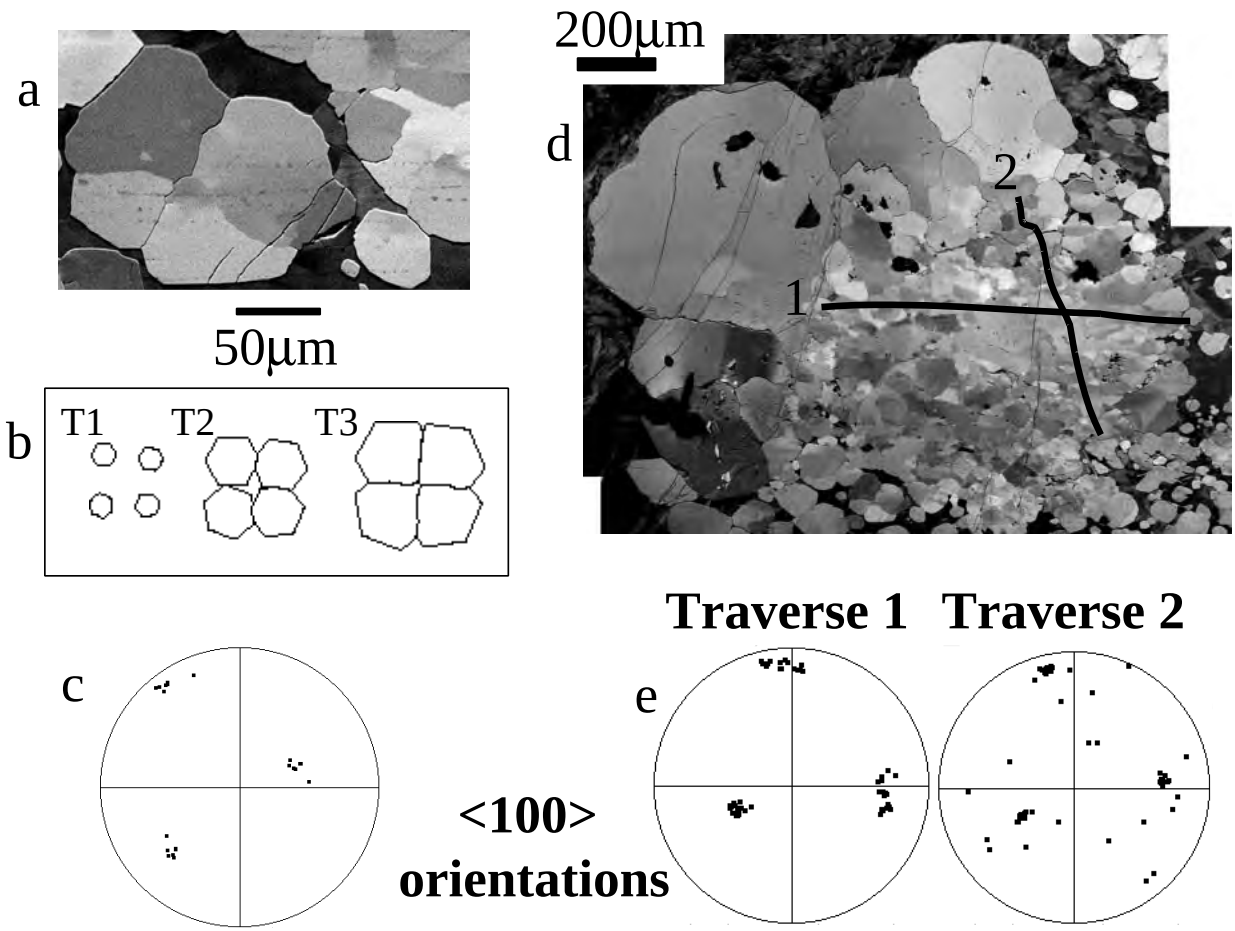

FIGURE 10. (**a**) OC image of a garnet comprising several orientations indicated by different shades of gray. The different shades of gray correspond to changes in facetting on the interphase boundary between garnet (generally pale) and other phases (darker). (**b**) Conceptual model of formation of the microstructure in 10a by nucleation and amalgamation of different garnets. (**c**) Plot of <100> axes from six different grey shade domains identified in the garnet cluster in Figure 10a. The individual garnets have very similar orientations but are not dispersed along small circle distributions as in Figure 8. (**d**) OC image montage giving a view of a larger area of garnet. The garnet cluster in a can be seen in the bottom center of this image. Solid lines 1 and 2 mark traverses of EBSD measurements (shown in 10e) across garnet. The grey shade variations crossed by the traverses show different garnet orientations. No other phases are involved along the traverse lines. (**e**) Plot of <100> axes from measurements along traverses 1 and 2 (shown in 10d). All the garnets have similar orientations but are not clearly dispersed along small circle distributions as in Figure 8.

that compares well with forward modeling of interface textures related to multiple random nucleation (Elliot 1998). The complicating factor is that the orientations of the garnet (Figs. 10c and 10e) measured from the sub-domains in Figures 10a and 10d are all very similar. The orientation data do not show any consistent rotation axes, as in the garnet in Figure 8. The nucleation and coalescence of the garnets remains the most likely model to explain the observed textures, but an additional control must be proposed to explain the common orientation of the garnets. Mimetic growth on a precursor mineral cannot be ruled out yet seems unlikely as there is no obvious candidate in these specimens. Coalescence of the nuclei may be controlled by some mechanism that favors aggregation of similarly oriented nuclei and destroys or reorients strongly misoriented ones. Such a process could be driven by a surface-energy mechanism, which is difficult to rationalize because the energy associated with chemical potential variations related to observed garnet zonation would be much more significant. Another alternative is that orientation at nucleation could be controlled by stress. If it can be shown that stress is an important control on porphyroblast nucleation, then some fundamentals of our understanding of metamorphic petrology will need re-appraisal. Whatever the final conclusion, one would not be able to address this problem without the data from EBSD and OC imaging.

Constraints on magmatic processes

Shape fabrics are a constraint on processes in magmatic rocks. However, direct measurements of shapes are slow and the 3D shape must be reconstructed from 3 orthogonal sets of 2D data or from serial sectioning or grinding. When minerals grow free of constraint, such as during the early stages of crystallization from magma, the shape of the crystals has a strong correlation with crystallography (Benn and Allard 1989). EBSD provides a simple, rapid method of assessing CPOs in igneous rocks. An example data set is shown in Figure 11. In cases such as this, where it is reasonable to assume that shapes and crystallography correspond, studies of the CPOs of elongate minerals may enable fundamental processes to be distinguished. Simple models predict that monoclinic CPOs would result from alignment during simple shear (such as in flow of a density current) whereas orthorhombic CPOs would result from settling. Compaction would modify further any depositional fabrics and may be identified from subgrain structures within grains. Comparative studies of the CPOs of elongate and equant minerals (olivine vs. magnetite for example) should enable processes associated with flow regimes to be distinguished from other processes, such as in situ crystallization.

Constraints on microsampling for geochemical analysis

Recent advances in our understanding of rock geochemistry and radiometric age dating stem from "microprobe" analyses that allow the determination of trace element and stable and radiogenic isotope compositions within individual mineral grains. Laser ablation is increasingly used to extract small volumes as are ion-beam techniques such as SHRIMP and SIMS (see Potts et al. 1995). Microdrilling techniques have also been employed to constrain intra-grain geochemistry.

The results of high spatial resolution geochemical sampling by these techniques in many cases are difficult to reconcile with the simple models of volume diffusion (Dodson 1973) that are commonly used to interpret intragrain geochemical variations. One potential reason for this is that intragrain microstructure may modify the diffusion characteristics of the grain or may

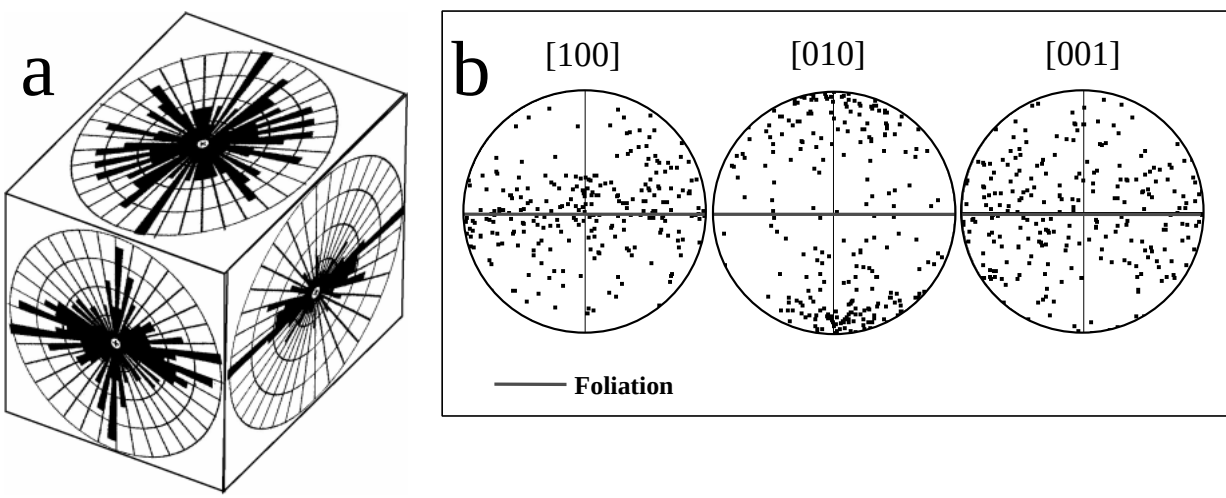

FIGURE 11. (**a**) Measurements of olivine shapes from three orthogonal planes in a Rum cumulate; data from Zetterström (1996). The foliation surface is the upper surface. (**b**) EBSD measurements (252 data points) of olivine CPO from one of the thin sections used to measure shapes in 11a. The CPO data and shape data suggest that olivines have [010] short axes that lie normal to foliation, but lack consistent orientation of long axes. The difference between the [100] and [001] plots suggest that this is because the long axes are scattered in the foliation plane rather than because the *a* axes and *c* axes have similar dimensions.

lead to the development of fast diffusion pathways and a diffusional anisotropy through the grain (Lee 1995). The effects of intragrain microstructure are difficult to resolve either because the microstructure of the samples cannot be resolved at the same scale as the geochemical analysis, or because the microstructural and geochemical samples require different preparation procedures thereby precluding geochemical and microstructural study on the same grain. Here we outline an example that illustrates the potential usefulness of the SEM in linking microstructural and geochemical studies.

The measurement of Ar isotopic ratios and their use in dating has been revolutionized by the development of laser microsampling techniques (York et al. 1981; Lee et al. 1991; Kelley et al. 1994). Such laser Ar studies have revealed considerable complexities in the distribution of $^{40}Ar/^{39}Ar$ ages within individual mineral grains and some of these complexities have been suggested to be due to grain microstructure (e.g., Burgess et al. 1992 for feldspar and Reddy et al. 1996 and Pickles et al. 1997 for micas). However these studies have found it difficult to correlate observed intragrain microstructure directly with Ar isotopic variations at the same scale or on the same samples. This is in part due to the fact that slabs used for in situ Ar dating are too thick for standard petrographic observations. However detailed maps of phase relationships using Z-contrast images have constrained intergrain microstructure sufficiently to enable different microstructural sites to be analysed (Reddy et al. 1996, 1997; Pickles et al. 1997). Further application of the OC SEM technique allows orientation contrast images of individual grains to be used to identify microstructural variations at the same scale as the Ar analyses. The results allow Ar age variations to be related to the proximity of orientation domain boundaries such as kinks, microfractures, and subgrain boundaries. The first results from an OC-laser Ar study (Reddy et al. 1999) show that the diffusion of Ar in potassium feldspar can be heterogeneous and related to deformation-induced microstructures within the feldspar (Fig. 12).

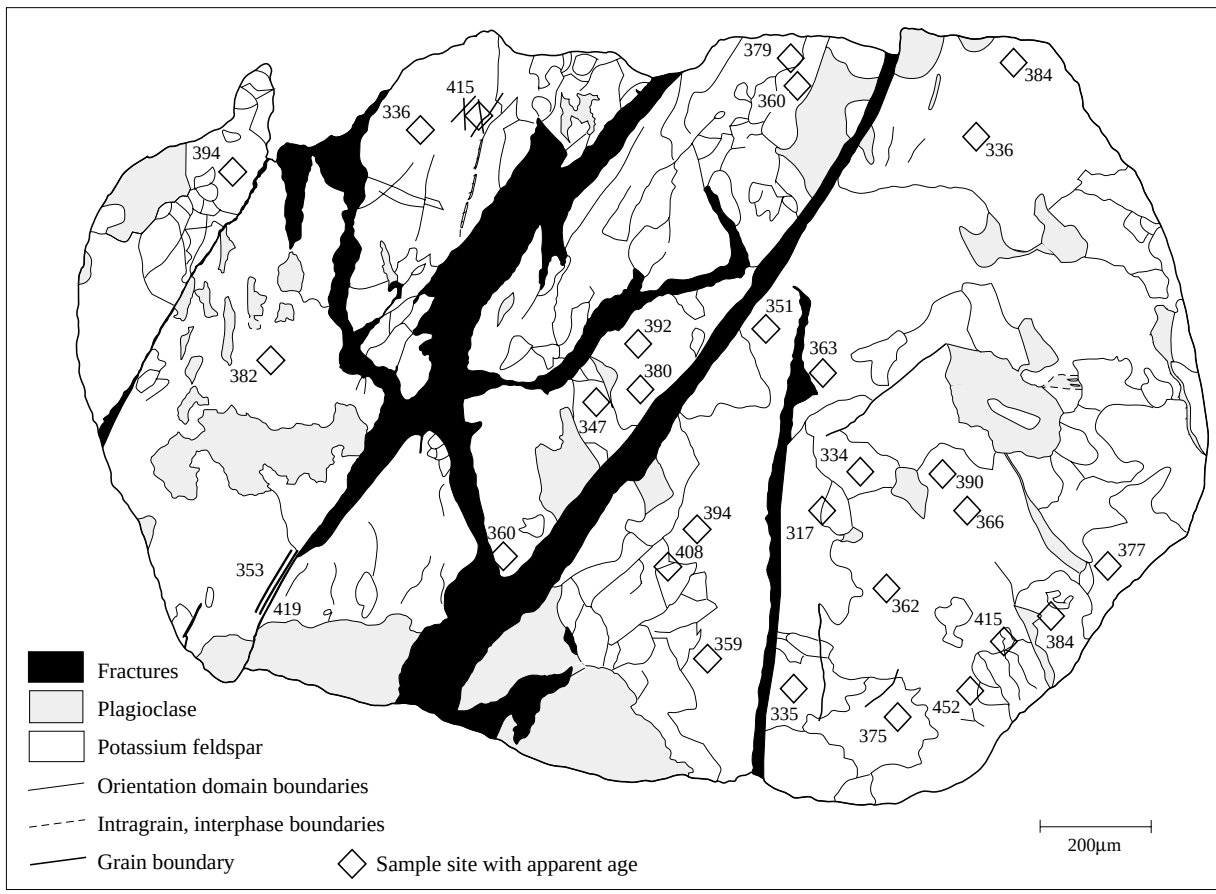

FIGURE 12. Microstructure of a naturally deformed potassium feldspar. The plagioclase-potassium-boundaries were resolved using Z-contrast images. The intra-potassium feldspar boundaries are orientation-contrast domain boundaries resolved using OC forescattered SEM. Note the strong association of relatively old $^{40}Ar/^{39}Ar$ ages with orientation domain boudaries.The ages are given in millions of years. The diamonds represent both the position and the size of the ablation pit. Modified from Reddy et al. (1999).

SUMMARY

(1) EBSD provides the easiest way to measure the full crystallographic orientation of individual rock-forming minerals of ≥1 μm in size.

(2) OC images provide maps of the misorientation boundaries in a specimen. These maps can be used to locate EBSD analysis points.

(3) Automated EBSD and orientation mapping is not yet possible for all rock-forming minerals, mainly because of misindexing. However orientation and misorientation maps can be constructed from OC images and EBSD data, and software and hardware developments are improving automated procedures rapidly.

(4) Charging problems are the likely cause of the low spatial resolution of EBSD work in non-conducting minerals (~1 μm with a W filament, ~0.25 μm with FEGSEM) compared with conducting metals (~60 μm with a W filament, ~30 μm with FEGSEM). Solving the charging problem is a current technical challenge.

(5) EBSD is not yet capable of accurately defining misorientation axes, across individual low-angle boundaries. Both SAECP and convergent beam TEM techniques give better results. Development of high-speed, high-angular resolution EBSD is a current technical challenge.

(6) EBSD and OC imaging have wide applications to petrology. Applications to the study of deformation microstructures are best established. Applications to metamorphic and magmatic rocks are likely to yield new insights into fundamental petrogenetic processes. These techniques are an important accompaniment to geochemical microsampling programs.

ACKNOWLEDGMENTS

Kees Veltkamp is thanked for his help in keeping the SEM unit operational. The work presented here has benefited from discussions with Dave Dingley, John Humphreys, Geoff Lloyd, Karsten Kunze, Dick Paden, Niels Henrik Schmidt and Angus Wilkinson. The majority of this paper was written in periods between field localities on an excursion in Chilean Patagonia. Les agreduzco á mis colegas científicos y á la tripulacíon del cutter '21 de Mayo', para mantener un ambiente tan relajante para escribir. Thorough journal reviews by Andy Barker and Ken Hickey were invaluable in identifying the most essential elements of what was a much longer manuscript. I thank Scott Johnson for his editorial patience.

REFERENCES CITED

Adams, B.L., Wright, S.I., and Kunze, K. (1992) Orientation imaging: the emergence of a new microscopy. Mettalurgical Transactions A, 24, 819–831.

Ashby, M.F. (1972) A first report on deformation mechanism maps. Acta Metallurgica, 20, 887–897.

Benn, K. and Allard, B. (1989) Preferred mineral orientations related to magmatic flow in ophiolite layered gabbros. Journal of Petrology, 30, 925–946.

Boyle, A.P., Burton, K.W., and Westhead, R.K. (1994) Diachronous burial and exhumation of a single tectonic unit during collision orogenesis (Sulitjelma, Central Scandinavian Caledonides). Geology, 22, 1043–1046.

Boyle, A.P., Prior, D.J., Banham, M.H., and Timms, N.E. (1998) Plastic deformation of metamorphic pyrite: new evidence from electron backscatter diffraction and forescatter orientation contrast imaging. Mineralium Deposita, 34, 71–81.

Brearley, A.J. (1987) A natural example of the disequilibrium breakdown of biotite at high temperature-TEM observations and comparison with experimental kinetic data. Mineralogical Magazine, 51, 93–101.

Brearley, A.J., Rubie, D.C., and Ito, E. (1992) Mechanisms of the transformations between the alpha-polymorphs, beta-polymorphs and gamma-polymorphs of Mg_2SiO_4 at 15 GPa. Physics and Chemistry of Minerals, 18, 343–358.

Bunge, H.J. (1982) Fabric analysis by orientation distribution functions. Tectonophysics, 78, 1.

Burgess, R., Kelley, S.P., Parsons, I., Walker, F.D.L., and Worden, R.H. (1992) 40Ar/39Ar analysis of perthite microtextures and fluid inclusions in alkali feldspars from the Klokken syenite, south Greenland. Earth and Planetary Science Letters, 109, 147–167.

Campbell, G.H., Foiles, S.M., Huang, H.C., Hughes, D.A., King, W.E., Lassila, D.H., Nikkel, D.J., de la Rubia, T.D., Shu, J.Y., and Smyshlyaev, V.P. (1998) Multi-scale modeling of polygonal plasticity: a workshop report. Material Science and Engineering, A251, 1–22.

Cook, N.J., Halls, C., and Boyle, A. P. (1993) Deformation and metamorphism of massive sulphides at Sulitjelma, Norway. Mineralogical Magazine, 57, 67–81.

Day, A. (1993) Developments in the EBSP technique and their application to grain imaging, Ph.D. dissertation, University of Bristol.

——(1998) Is that one grain or two? Materials World, January, 1998, 8–10.

Day, A. and Quested, T.E. (1999) A comparison of grain imaging using HOCI, COCI, EBSP and optical methods. Journal of Microscopy, 195, 186–196.

Dingley, D.J. (1984) Diffraction from sub-micron areas using electron backscattering in a scanning electron microscope. Scanning Electron Microscopy, 2, 569–575.

——(1989) Developments in on-line crystal orientation determination. Institute of Physics Conference Series, 98, 473–476.

Dodson, M.H. (1973) Closure temperature in cooling geochronological and petrological systems. Contributions to Mineralogy and Petrology, 40, 259–274.

Elliot, M. (1998) The three dimensional numerical simulation of crystallizing media, 85 p. Ph.D. dissertation, University of Liverpool.

Etchecopar, A. (1977) A plane kinematic model of progressive deformation in a polycrystalline aggregate. Tectonophysics, 39, 121–139.

Farmer, A.B. (1992) A microstructural investigation of natural deformation in quartz aggregates, 307p. Ph.D. dissertation, University of Leeds.

Faul, U.H. and Fitz Gerald, J.D. (1999) Grain misorientations in partially molten olivine aggregates: an electron backscatter diffraction study. Physics and Chemistry of Minerals, in press.

Field, D.P. (1997) Recent advances in the application of orientation imaging. Ultramicroscopy, 67, 1–9.

Fliervoet, T.F. (1995) Deformation mechanisms in fine-grained quartzo-feldspathic mylonites. An electron microscope study. Geologica Ultraiectina, 131, University of Utrecht, 167.

Fliervoet, T.F., White, S.H., and Drury, M.R. (1997) Evidence for dominant grain-boundary sliding deformation in greenschist and amphibolite grade polyminerallic ultramylonites from the Redbank deformed zone, Central Australia. Journal of Structural Geology, 19, 1495–1520.

Fliervoet, T.F., Drury, M.R., and Chopra, P.N. (1999) Crystallographic preferred orientations and misorientations in some olivine rocks deformed by diffusion or dislocation creep. Tectonophysics, 303, 1–27.

Frank, F.C. (1988) Orientation mapping. Metallurgical Transactions, 19A, 403–408.

Frost, H.J. and Ashby, M.F. (1982) Deformation mechanism maps: the plasticity and creep of metals and ceramics, 166 p. Pergamon Press, Oxford.

Fynn, G.W. and Powell, W.J.A. (1979) The cutting and polishing of electro-optic materials, 216 p. Adams Hilger, London.

Goldstein, J.I., Newbury, D.E., Echlin, P., Joy, D.C., Romig, A.D. Jr., Lyman, C.E., Fiori, C., and Lifshin, E. (1992) Scanning electron microscopy and X-Ray microanalysis (second edition), 820 p. Plenum Press, New York.

Goodhew, P.J. and Humphreys, F.J. (1988) Electron Microscopy and Analysis, 232p. Taylor and Francis, Bristol.

Green, D.J. (1998) An introduction to the mechanical properties of ceramics, 336 p. Cambridge University Press, Cambridge.

Hirth, G. and Tullis, J. (1992) Dislocation creep regimes in quartz aggregates. Journal of Structural Geology, 14, 145–159.

Humphreys, F.J. (1997) A unified theory of recovery, recrystallization and grain growth, based on the stability and growth of cellular microstructures-I The basic model. Acta Materialia, 10, 4231–4240.

Humphreys, F.J. (1999) Quantitative metallography by electron backscatter diffraction. Journal of Microscopy, 195, 170–185.

Humphreys, F.J. and Hatherly, M. (1995) Recrystallization and related annealing phenomena, 497 p. Pergamon Press, Oxford.

Humphreys, F.J., Huang, Y., Brough, I., and Harris, C. (1999) Electron backscatter diffraction of grain and subgrain structures—resolution considerations. Journal of Microscopy, 195, 212–216.

Jessell, M.W. (1988) Simulation of fabric development in recrystallizing aggregates-I Description of the model. Journal of Structural Geology, 10, 771–778.

Joy, D.C. (1974) Electron channeling patterns in the SEM. in Holt, D.B., Muir, M.D., Boswarva, I.M., and Grant, P.R. Quantitative Scanning Electron Microscopy, Academic Press, New York.

Juul Jensen, D. and Schmidt, N.H. (1990) An automatic on-line technique for determination of crystallographic orientation by EBSP. In P. Chandra, Ed., Proceedings, Recrystallization 90. 219–224.

Kelly, S.P., Arnaud, N.O., and Turner, S.P. (1994) High spatial resolution $^{40}Ar/^{39}Ar$ investigations using an ultraviolet laserprobe extraction technique. Geochemica Cosmochemica Acta, 58, 3519–3525.

Knipe, R.J. (1989) Deformation mechanisms, recognition from natural tectonites. Journal of Structural Geology, 11, 127–146.

Koch, P.S. (1983) Rheology and microstructures of experimentally deformed quartz aggregates, Ph.D. dissertation, University of California.

Krieger-Lassen, N.C. (1996) The relative precision of crystal orientations measured from electron backscattering patterns. Journal of Microscopy, 181, 72–81.

——(1998) Automatic high-precision measurements of the location and width of Kikuchi bands in electron backscatter diffraction patterns. Journal of Microscopy, 190, 375–391.
Krieger-Lassen, N.C., Juul Jensen, D., and Conradson, K. (1992) Image-processing procedures analysis of electron backscattering patterns. Scanning Microscopy, 6, 115–121.
Kruhl, J.H. (1996) Prism and basal-plane subgrain boundaries in quartz: a microstructural geothermobarometer. Journal of Metamorphic Geology, 14, 581–589.
Kruhl, J.H. and Nega, M. (1996) The fractal shape of sutured quartz grain boundaries: application as a geothermometer. Geologische Rundschau, 85, 38–43.
Law, R.D. (1987) Heterogeneous deformation and quartz crystallographic fabric transitions-natural examples from the Moine thrust zone at the Stack of Glencoul, Northern Assynt. Journal of Structural Geology, 9, 819–833.
——(1990) Crystallographic fabrics: a selective review of their applications to research in structural geology. In R.J. Knipe, and E.H. Rutter, Eds., Deformation mechanisms, rheology and tectonics. Geological Society of London Special Publication, 54, 335–352.
Law, R.D., Knipe, R.J., and Casey, M. (1986) Kinematic and tectonic significance of microstructures and crystallographic fabrics within quartz mylonites from the Assynt and Eriboll regions of the Moine thrust zone, NW Scotland. Transactions of the Royal Society of Edinburgh: Earth Sciences, 77, 99–125.
Law, R.D., Schmid, S.M., and Wheeler, J. (1990) Simple shear deformation and quartz crystallographic fabrics: a possible natural example from the Torridon area of NW Scotland. Journal of Structural Geology, 12, 29–45.
Lee, J.K.W. (1995) Multipath diffusion in geochronology. Contributions to Mineralogy and Petrology, 10, 60–82.
Lee, J.K.W., Onstott, T.C., Cashman, K.V., Cumbest, R.J., and Johnson, D. (1991) Incremental heating of hornblende in vacuo: implications for $^{40}Ar/^{39}Ar$ geochronology and the interpretation of thermal histories. Geology, 19, 872–876.
Leiss, B. and Barber, D. (1999). Mechanisms of dynamic recrystallization in naturally deformed dolomite inferred from EBSP analyses. Tectonophysics, 303, 51–69.
Lister, G.S., Paterson, M., and Hobbs, B.E. (1978) The simulation of fabric development during plastic deformation and its application to quartzite: the model. Tectonophysics, 45, 107–158.
Lloyd, G.E. (1985) Review of instrumentation, techniques and applications of SEM in mineralogy. In J.C. White, Ed., Applications of electron microscopy in Earth Sciences. Mineralogical Association of Canada short course 11, 151–188.
——(1987) Atomic number and crystallographic contrast images with the SEM: A review of backscattered techniques. Mineralogical Magazine, 51, 3–19.
——(1994) An appreciation of the SEM electron channeling technique for microstructural analysis of geological materials. In H.J. Bunge, S. Siegesmunde, W. Skrotzki, and K. Weber, Eds., Textures of geological materials, p. 109–126. DGM Informationgesellschaft Verlag, Oberursel.
Lloyd, G.E. and Ferguson, C.C. (1986) A spherical electron-channeling pattern map for use in quartz petrofabric analysis. Journal of Structural Geology, 8, 517–526.
Lloyd, G.E. and Freeman, B. (1991) SEM electron channeling analysis of dynamic recrystallization in a quartz grain. Journal of Structural Geology, 13, 945–953.
——(1994) Dynamic recrystallization of quartz and quartzites. Journal of Structural Geology, 16, 867–881.
Lloyd, G.E. and Knipe, R.J. (1992) Deformation mechanisms accommodating faulting of quartzite under upper crustal conditions. Journal of Structural Geology, 14, 127–143.
Lloyd, G.E., Ferguson, C.C., and Law, R.D. (1987) Discriminatory petrofabric analysis of quartz rocks using SEM electron channeling. Tectonophysics, 135, 243–249.
Lloyd, G.E., Schmidt, N.H., Mainprice, D., and Prior, D.J. (1991) Crystallographic textures. Mineralogical Magazine, 55, 331–345.
Lloyd, G.E., Law, R.D., Mainprice, D., and Wheeler, J. (1992) Microstructural and crystal fabric evolution during shear zone formation. Journal of Structural Geology, 14, 1079–1100.
Lloyd, G.E., Farmer, A.B., and Mainprice, D. (1997) Misorientation analysis and the formation and orientation of subgrain and grain boundaries. Tectonophysics, 279, 55–78.
Loretto, M.H. (1994) Electron beam analysis of materials (second edition), 272 p. Chapman and Hall, London.
MATTER: Materials Science on CD ROM v 2.1. University of Liverpool Press. http://www.liv.ac.uk/~matter/home.html.
McClaren, A.C. (1986) Some speculations on the nature of high angle grain boundaries in quartz rocks. In B.E. Hobbs and H.C. Heard, Eds., Mineral and Rock Deformation: Laboratory Studies, AGU Geophysical Monographs 36, AGU, 233–245.
——(1991) Transmission electron microscopy of minerals and rocks, 223 p. Cambridge University Press, Cambridge.
McClay, K.R. and Ellis, P.G. (1983) Deformation and recrystallization of pyrite. Mineralogical Magazine, 47, 527–538.
McDonnell., R.D. (1997) Deformation of fine-grained synthetic peridotite under wet conditions, 195 p. Geologica Ultraiectina, 152, University of Utrecht.
Means, W.D. (1981) The concept of steady state foliation. Tectonophysics, 78, 179–199.
Mercier, J.C.C., Anderson, D.A., and Carter, N.L. (1977) Stress in the lithosphere. Interferences from steady state flow of rocks. Pure and Applied Geophysics, 115, 199–226.
Nichols, C.S., Cook, R.F., Clarke, D.R., and Smith, D.A. (1991) Alternative length scales for polycrystalline materials-I. Microstructure evolution. Acta metallergica materialia, 39, 1657–1666.
Nishikawa, S. and Kikuchi, S. (1928) Diffraction of cathode rays by mica. Nature, 121, 1019–1020.
Passchier, C.W. and Trouw, R.A.J. (1996) Microtectonics, 289 p. Springer Verlag, Berlin.
Pickles, C.S., Kelley, S.P., Reddy, S.M., and Wheeler, J. (1997) Determination of high spatial resolution argon isotope variations in metamorphic biotites. Geochimica Cosmochimica Acta, 61, 3809–3833.
Pospiech, J., Sztwiertnia, K., and Haessner, F. (1986) The misorientation distribution function. Textures and Microstructures, 6, 201.
Potts, P.J., Bowles, J.F.W., Reed, S.J.B., and Cave, M.R. (1995) Microprobe techniques in the Earth Sciences. Chapman and Hall, 419 p.
Prior, D.J. (1992) Sub-critical fracture and associated retrogression of garnet during mylonitic deformation. Contributions to Mineralogy and Petrology, 113, 545–556.
——(1999) Problems in determining the orientations of crystal misorientation axes, for small angular misorientations, using electron backscatter diffraction in the SEM. Journal of Microscopy, 195, 217–225.
Prior, D.J. and Wheeler, J. (1999) A study of an albite mylonite using electron backscatter diffraction. Tectonophysics, 303, 29–49.
Prior, D.J., Knipe, R.J., and Handy, M.R. (1990) Estimates of rates of microstructural changes in mylonites. In R.J. Knipe, and E.H. Rutter, Eds., Deformation mechanisms, rheology and tectonics. Geological Society of London Special Publication, 54, 309–320.
Prior, D.J., Trimby, P.W., Weber, U.D., and Dingley, D.J. (1996) Orientation contrast imaging of microstructures in rocks using forescatter detectors in the scanning electron microscope. Mineralogical Magazine, 60, 859–869.
Pryer, L.L., Lloyd, G.E., and Robin, P.Y.F. (1995) An SEM electron-channeling study of flame perthite from the Killarney Granite, Southwestern Grenville Front, Ontario. Canadian Mineralogist, 33, 333–347.
Putnis, A. (1992) Introduction to mineral sciences, 457 p. Cambridge University Press, Cambridge.
Randle., V. (1992) Microtexture determination and its applications, 174 p. The Institute of Materials, London.
——(1994) Application of electron backscatter diffraction to steel products. Ironmaking and Steelmaking, 21, 209–214.
——(1995) An investigation of grain-boundary plane crystallography in polycrystalline nickel. Journal of Materials Science, 30, 3983–3988.
Randle, V. and Caul, M. (1996) Representation of electron backscatter diffraction data. Materials Science and Technology, 12, 844–850.
Randle, V. and Dingley, D.J. (1989) Measurement of boundary plane inclination in a scanning electron microcope. Scripta Metallurgica, 23, 1565–1570.
Reddy, S.M., Kelley, S.P., and Wheeler, J. (1996) A $^{40}Ar/^{39}Ar$ laser probe study of micas from the Sesia zone, Italian Alps: implications for metamorphic and deformation histories. Journal of Metamorphic Geology, 14, 493–508.
Reddy, S.M., Kelley, S.P., and Magennis, L. (1997) A microstructural and argon laserprobe study of shear zone development at the western margin of the Nanga Parbat-Haramosh Massif, western Himalaya. Contributions to Mineralogy and Petrology, 128, 16–29.
Reddy, S.M., Potts, G.J., Kelley, S.P., and Arnaud, N. (1999) The effects of deformation-induced microstructures on intragrain argon isotope ages in feldspars. Geology, 27, 363–366.
Reimer, L., Heilers, U., and Saliger, G. (1996) Kikuchi band contrast in diffraction patterns recorded by transmitted and backscattered electrons. Scanning, 8, 101–118.
Rowe, K.J. and Rutter, E.H. (1990) Palaeostress estimation using calcite twinning,: experimental calibration and application to nature. Journal of Structural Geology, 12, 1–17.
Rubie, D.C. and Brearley, A.J. (1994) Phase-transitions between beta-$(Mg,Fe)_2SiO_4$ and gamma-$(MgFe)(2)SiO_4$ in the earths mantle-mechanisms and rheological implications. Science, 264, 1445–1448.
Rutter, E.H. (1995) Experimental study of the influence of stress, temperature and strain on the dynamic recrystallization of Carrara marble. Journal of Geophysical Research, 100, 24651–24663.
——(1998) The use of extension testing to investigate the high strain rheological behaviour of marble. Journal of Structural Geology, 20, 243–254.
Sander, B. (1930) Gefügekunde der Gesteine. Springer, Berlin.
——(1970) An introduction to the study of fabrics of geological bodies, 641 p. Pergamon Press, Oxford.
Schmid, S.M. and Casey, M. (1986) Complete fabric analysis of some commonly observed quartz c-axis patterms. In B.E. Hobbs and H.C. Heard Eds., Mineral and Rock Deformation: Laboratory Studies, AGU Geophysical Monographs 36, AGU, 263–286.
Schmid, S.M., Casey, M., and Starkey, J. (1981) An illustration of the advantages of a complete texture analysis described by the orientation distribution function (ODF) using quartz pole figure data. Tectonophysics, 78, 101–117.

Schmidt, N.H. and Olesen, N.O. (1989) Computer-aided determination of crystal lattice orientation from electron channeling patterns in the SEM. Canadian Mineralogist, 27,15–22.

Schwarzer, R.A. (1997) Automated crystal lattice orientation mapping using a computer-controlled SEM. Micron, 28, 249–265.

Schwarzer, R.A. and Weiland, H. (1988) Texture analysis by the measurement of individual grain orientations-electron microscopical methods and applications on dual phase steel. Textures and Microstructures, 8-9, 551–557.

Spry, A. (1969) Metamorphic textures, 352 p. Pergamon Press, Oxford.

Takahashi, M., Nagahama, H., Masuda, T., and Fujimura, A. (1998) Fractal analysis of experimentally, dynamically recrystallized quartz grains and its possible applications as a strain rate meter. Journal of Structural Geology, 20, 269–275.

Tanaka, M., Kazama, A., Ito, Y., and Kato, R. (1998) Effects of the creep deformation on the fractal dimension of grain boundaries in austentite steels. Journal of Material Science, 33, 3351–3359.

Trimby, P.W. (1998) Quantifying microstructures—the development and application of a new technique to a quartzitic shear zone, 125 p. Ph.D. dissertation, University of Liverpool.

Trimby, P.W. and Prior, D.J. (1999) Microstructural imaging techniques: a comparison of optical and scanning electron microscopy in the study of deformed rocks. Tectonophysics, 303, 71–81.

Trimby, P.W., Prior, D.J., and Wheeler, J. (1998) Grain boundary hierarchy development in a quartz mylonite. Journal of Structural Geology, 20, 917–935.

Twiss, R.J. (1977) Theory and applicability of a recrystallized grainsize palaeopiezometer. Pure and Applied Geophysics, 115, 227–224.

——(1986) Variable sensitivity piezometric equations for dislocation density and subgrain diameter and their relevance to olivine and quartz. In B.E. Hobbs and H.C. Heard, Eds., Mineral and Rock Deformation: Laboratory Studies, AGU Geophysical Monographs 36, AGU, 247–263.

Venables, J.A. and Harland, C.J. (1973) Electron backscattering patterns-a new technique for obtaining crystallographic information in the SEM. Philosophical Magazine, 27, 1193–1200.

Wenk, H.R. and Christie, J.M. (1991) Comments on the interpretation of deformation textures in rocks. Journal of Structural Geology, 13:1091–1110.

Wheeler, J. (1987) The significance of grain-scale stresses in the kinetics of metamorphism. Contributions to Mineralogy and Petrology, 97, 397–404.

Wenk, H.R. and Kocks, U.F. (1987) The representation of orientation distributions. Metallurgical Transactions, 18A, 1083.

Wheeler, J. (1991) A view of texture dynamics. Terra Nova, 3, 123–136.

——(1992) The importance of pressure solution and Coble creep in the deformation of polymineralic rocks. Journal of Geophysical Research, 97, 4579–4586.

Wilkinson, A.J. (1996) Measurement of elastic strains and small lattice rotations using electron back scatter diffraction. Ultramicroscopy, 62, 237–247.

——(1997) Methods for determining elastic strains from electron backscatter diffraction and electron channeling patterns. Materials Science and Technology, 13, 79–84.

Wilkinson, A.J. and Hirsch, P.B. (1997) Electron diffraction based techniques in scanning electron microscopy of bulk materials. Micron, 28, 279–308.

Wilkinson, A.J., Anstis, G.R., Czernuska, J.T., Long, N.J., and Hirsch, P.B. (1993) Electron channeling contrast imaging of interfacial defects in strained silicon-germanium layers on silicon. Philosophical Magazine, 68, 59–80.

Worden, R.H., Champness, P.E., and Droop, G.T.R. (1987) Transmission electron microscopy of the pyrometamorphic breakdown of phengite and chlorite, Mineralogical Magazine, 51, 107–111.

Worden, R.H., Droop, G.T.R., and Champness, P.E. (1991) the reaction antigorite-olivine + talc + H_2O in the Bergell aureole, N Italy. Mineralogical Magazine, 55, 367–377.

Wright, S.I. and Adams, B.L.A. (1992) Automatic analysis of electron backscatter diffraction patterns. Metallurical Transactions, 23A, 759–767.

Wright, S.I., Adams, B.L.A., and Kunze, K. (1993) Application of a new automatic lattice orientation measurement technique to polycrystalline alumnium. Materials Science and Engineering, A160, 229–240.

York, D., Hall, C.M., Yanase, Y., Hanes, J.A., and Kenyon, W.J. (1981) $^{40}Ar/^{39}Ar$ dating of terrestrial minerals with a continuous laser. Journal of Geophysical Research, 8, 1136–1138.

Zetterström, L. (1996) Fabric studies of layered igneous rocks from Rum, Scotland, 69p. M.Sc. dissertation, Stockholm University.

MANUSCRIPT RECEIVED NOVEMBER 30, 1998
MANUSCRIPT ACCEPTED JUNE 30, 1999
PAPER HANDLED BY SCOTT E. JOHNSON